PAPER • OPEN ACCESS

Effects of drifts on scrape-off layer transport in W7-X

OPEN ACCESS
IOP Publishing | International Atomic Energy Agency Nuclear Fusion
Nucl. Fusion **63** (2023) 026022 (18pp) https://doi.org/10.1088/1741-4326/acab75

Effects of drifts on scrape-off layer transport in W7-X

D.M. Kriete[1,*], A. Pandey[2], V. Perseo[2], J.C. Schmitt[1], D.A. Ennis[1], D. Gradic[2], K.C. Hammond[3], M. Jakubowski[2], C. Killer[2], R. König[2], D.A. Maurer[1], F. Reimold[2], V. Winters[2], M.N.A. Beurskens[2], S.A. Bozhenkov[2], K.J. Brunner[2], G. Fuchert[2], J. Knauer[2], E. Pasch[2], E.R. Scott[2] and the W7-X Team[2,a]

[1] Auburn University, Auburn, AL, United States of America
[2] Max-Planck-Institut für Plasmaphysik, Greifswald, Germany
[3] Princeton Plasma Physics Laboratory, Princeton, NJ, United States of America

E-mail: kriete@auburn.edu

Received 13 September 2022, revised 31 October 2022
Accepted for publication 14 December 2022
Published 6 January 2023

Abstract

Drifts affect particle, momentum, and energy transport in the scrape-off layer (SOL) of tokamaks and stellarators, altering plasma flows and creating asymmetries between divertors. To understand how drifts affect SOL transport in the W7-X island divertor, an experiment was performed to compare plasmas with matched core parameters but opposite magnetic field directions, and therefore opposite drift transport directions. Parallel flow measurements made with coherence imaging spectroscopy are interpreted with the aid of a diagnostic forward model and a 1D simple SOL model that includes the $\mathbf{E}\times\mathbf{B}$ drift. In low-density plasmas ($\overline{n}_e < 2\times10^{19}$ m^{-3}), the poloidal $\mathbf{E}\times\mathbf{B}$ drift induces a large poloidal density asymmetry within the island SOL, as measured by divertor Langmuir probes. This in turn causes the parallel flow stagnation point to shift from the position halfway between targets to the X-point in the drift direction, leading to near-unidirectional flow throughout the SOL. As density increases, the effects of the poloidal $\mathbf{E}\times\mathbf{B}$ drift decrease substantially, resulting in a smaller density asymmetry and the development of a counter-streaming flow pattern. For the entire density range probed in this experiment ($\overline{n}_e = 1.5-6\times10^{19}$ m^{-3}), the experimental observations are more consistent with the effects of the poloidal $\mathbf{E}\times\mathbf{B}$ drift than the radial $\mathbf{E}\times\mathbf{B}$ drift.

Supplementary material for this article is available online

Keywords: stellarator, scrape-off layer, island divertor, drifts, plasma flows, coherence imaging spectroscopy, divertor asymmetries

(Some figures may appear in colour only in the online journal)

* Author to whom any correspondence should be addressed.
[a] See Sunn Pedersen *et al* 2022 (https://doi.org/10.1088/1741-4326/ac2cf5) for the W7-X Team.

1. Introduction and motivation

A key mission of the Wendelstein 7-X (W7-X) stellarator [1, 2] is to assess the reactor viability of the island divertor [3, 4] heat and particle exhaust concept. To be successful in this regard, the island divertor must (a) spread out or dissipate the heat from the plasma enough to avoid overloading plasma-facing components (PFCs), (b) keep erosion of the PFCs at a sufficiently low level, (c) avoid excessive impurity transport into the core plasma, and (d) build up adequate neutral pressure to allow efficient pumping of particles. Achieving these requirements simultaneously is a major challenge, and doing so will require a good understanding of the physics governing plasma transport in the island divertor scrape-off layer (SOL).

The SOL contains magnetic field lines that are open and intersect PFCs. Heat and particles that escape the main confined plasma by crossing the last closed flux surface (LCFS) can then reach the PFCs via parallel transport along field lines or perpendicular transport across them. The ratio of parallel to perpendicular transport is a key parameter that governs the behavior of the edge plasma. It is one of the main differences between tokamak divertors, where parallel transport tends to dominate, and stellarator divertors, where perpendicular transport plays a comparatively more important role [5]. Parallel transport mechanisms are classical while perpendicular transport consists of an 'anomalous' component caused by turbulence and/or filaments, and an additional component arising from the $\mathbf{E}\times\mathbf{B}$ and diamagnetic drifts.

Drift-induced perpendicular transport can have important effects on the edge plasma. In tokamaks drifts contribute substantially to asymmetries of the electron temperature, density, radiation profiles, particle fluxes, and heat fluxes between inner and outer divertor legs [6–11] and have been shown to affect the dynamics of the transition from the attached to detached divertor state [12]. SOL drift effects in stellarators are less well understood, but initial studies on LHD [13], W7-AS [14], and W7-X [15] have observed similar drift-induced asymmetries between otherwise symmetric divertor targets. In W7-X, which uses toroidally discontinuous divertor targets, it was also observed that drifts drive heat loads onto 'shadowed' regions of the targets that are not typically expected to receive direct plasma heat flux [15]. Consequently, an additional practical motivation for understanding SOL drifts is that they must be sufficiently well-understood to ensure that they do not drive excessive heat loads onto peripheral PFCs.

Modeling the effects of drifts on the edge plasma is challenging. Two-dimensional codes applicable to the tokamak SOL such as UEDGE [16] and SOLPS [17] include drifts, but they are not always turned on in simulations due to computational cost, especially when drift effects are not the primary focus of investigation. Drift modeling in stellarators is in its infancy: there are currently no 3D SOL codes with plasma-neutral coupling that self-consistently include drifts, although recently a two-fluid edge turbulence code that includes drifts but not neutrals has been developed [18]. Efforts are underway to add drifts to EMC3-Eirene [19], the primary SOL code used to model W7-X, but a functional implementation is not complete. For this reason, SOL drift investigations in stellarators must currently be performed experimentally, with aid from simplified models. Furthermore, experimental drift investigations provide a dataset useful for future validation of 3D SOL codes.

In this paper, we present the results of an experimental investigation into drift effects on SOL transport in the W7-X island divertor. This work builds on the initial investigation in [15] by including new flow measurements throughout the SOL and interpreting the measurements using a simple SOL model that includes the $\mathbf{E}\times\mathbf{B}$ drift. In section 2, the experimental methodology is described and basic flow measurements are presented. Section 3 explains the diagnostic forward model used to help interpret the flow measurements. In section 4, a simple SOL drift model is developed and a basic physics picture of how drifts alter SOL parallel flows is introduced. Section 5 presents parallel flow and density asymmetry measurements and discusses how they are caused by the poloidal $\mathbf{E}\times\mathbf{B}$ drift.

2. Experimental setup and basic observations

To investigate the effects of drifts on SOL transport, an experiment was carried out during the OP1.2b run campaign of W7-X where pairs of discharges were created with matched core plasma parameters but oppositely directed magnetic fields. Reversing the magnetic field reverses the direction of drift-induced perpendicular transport, but does not directly affect parallel transport or anomalous perpendicular transport. Investigating the differences between these matched discharge pairs elucidates the role drifts play in SOL transport. The details of this experiment were previously described in [15]; we describe them again here for the sake of completeness.

2.1. Edge magnetic topology

The experiment was performed in the so-called 'low-iota' magnetic configuration (specifically the DBM configuration), which exhibits a single edge island with toroidal mode number $n=5$ and poloidal mode number $m=6$. As depicted in figure 1, this island surrounds the confined plasma, closing on itself after completing six toroidal and five poloidal transits around the machine. It is intersected by ten divertor targets made of graphite, forming the plasma-material interface. The low-iota magnetic configuration was chosen for this experiment because (a) it has the longest connection lengths of any of the main magnetic configurations in W7-X [20], maximizing the impact of drifts; (b) it is the configuration least affected by error fields, as the edge island is non-resonant with the dominant $n=1$ and $n=2$ error fields; and (c) in this configuration the divertor Langmuir probes have good coverage of the plasma-target interaction zone.

The edge plasma is divided into topologically separate regions that have different transport behavior. These regions

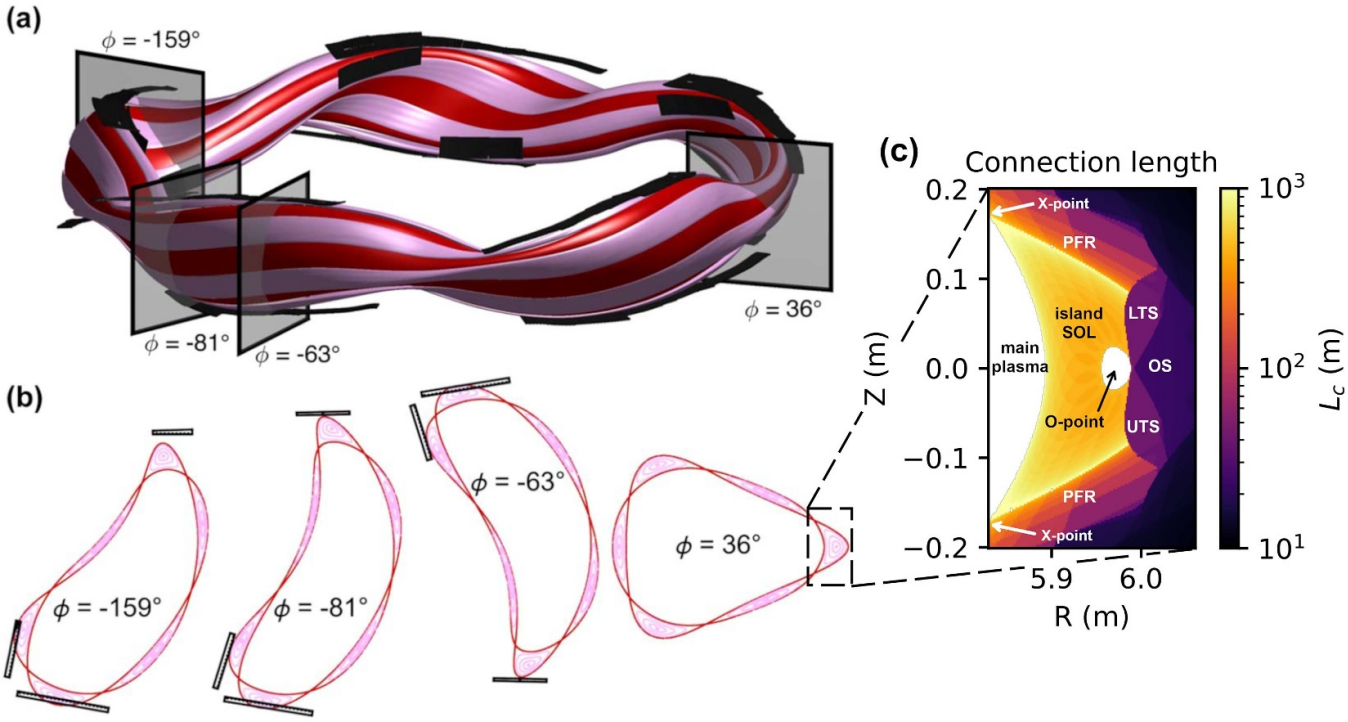

Figure 1. (*a*) W7-X plasma geometry for the low-iota magnetic configuration, showing the last closed flux surface of the main plasma (red) surrounded by an edge magnetic island (pink) that intersects the ten divertor targets (black), forming the scrape-off layer (SOL). (*b*) Poloidal cross-sections of the island at several toroidal angles. (*c*) Distribution of target-to-target connection lengths L_c throughout the edge plasma at $\phi = 36°$, which reveals several distinct topological regions: the island SOL, private flux region (PFR), O-point, lower target shadowed (LTS) region, upper target shadowed (UTS) region, and outer shadowed (OS) region. (*a*) and (*b*) reproduced from [15].

are evident in figure 1(*c*), which shows the distribution of target-to-target connection lengths L_c at the $\phi = 36°$ toroidal angle, where the island is in the gap between the toroidally discontinuous divertor targets. The connection lengths are calculated using the W7-X webservices field-line tracer [21] with vacuum fields only, i.e. neglecting the effects of finite β, toroidal current, and magnetic-force-induced coil deformation on the edge magnetic structure.

There are four main topological regions distinguished by stark differences in L_c: the island SOL, O-point, private flux region (PFR), and shadowed region. The island SOL is the part of the island in contact with the main confined plasma and is characterized by $L_c = 450-1700$ m. The PFR is outside the island and characterized by intermediate L_c values of 60−400 m. The shadowed region is the portion of the island that is cut by the divertor targets and has the shortest connection lengths in the edge. The shadowed region is further subdivided based on which divertor targets cut the island. Moving radially away from the LCFS toward the outboard side of the island, it is first cut by either two lower targets or two upper targets, forming the lower target shadowed (LTS) and upper target shadowed (UTS) regions, respectively. These regions have $L_c = 42$ m, corresponding to $L_c/(2\pi R_0) = (42\text{ m})/(35\text{ m}) = 1.2$ toroidal transits. Moving further radially, the island is eventually cut by both an upper and lower target, forming the outer shadowed (OS) region, which has $L_c \approx$ 20 m (0.6 toroidal transits). Finally, there is a small region of closed field lines around the island O-point.

Each topological region is magnetically isolated from its neighbors, so heat and particles can only cross between regions via perpendicular transport. Being in contact with the main plasma, the island SOL receives most of the heat and particle exhaust. Its boundary has the largest connection lengths, $L_c \approx$ 1000 m (≈30 toroidal transits), and forms the parallel heat exhaust channel. The PFR only contacts the main plasma at the X-points, so perpendicular transport from the island SOL is an important source for the PFR. The O-point and shadowed regions do not contact the main plasma at all, so perpendicular transport from the island SOL and PFR are their only source of heat and particles. Therefore, any field-reversal-induced plasma parameter changes in the shadowed region or the zone where it intersects the divertors are highly likely to be caused by drifts.

2.2. Methodology

The experiment was performed by creating pairs of discharges with opposite magnetic field direction but otherwise as closely matched as possible. Note that in W7-X, reversing the field direction does not change the SOL magnetic topology, unlike in a tokamak, where reversing the field direction alters the SOL magnetic topology unless the plasma

current is also reversed. The line-averaged electron density $\overline{n}_e$ and electron cyclotron resonance heating power P_{ECRH} were scanned on a discharge-to-discharge basis to investigate drift effects over a broad SOL parameter range. The scan covered $\overline{n}_e = 1.5{-}6.0 \times 10^{19}$ m^{-3} and $P_{ECRH} = 2{-}5$ MW. Within each discharge, the plasma parameters were ramped up during the first second and then held constant to the best extent possible throughout the remainder of the discharge, typically 4 s.

Example time traces of matched forward and reverse field discharges for low and high density cases with high power are shown in figure 2. The core plasma parameters $\overline{n}_e$ and diamagnetic stored energy W_{dia} are matched to better than 20% during the stationary phase (marked by the shaded regions), with deviations resulting from slow oscillations of $\overline{n}_e$ about its setpoint. The toroidal current I_{tor} is not as well-matched, and it increases continuously throughout the discharge, never reaching the full bootstrap current because the discharge length is shorter than the ~10 s decay time of the shielding current [22]. In contrast to the core plasma parameters, the C^{2+} impurity flow velocity $v_{C^{2+}}$ measured in the SOL near one of the island X-points changes dramatically upon field reversal, indicating that drifts have a substantive impact on SOL parameters.

For each discharge in the experiment, an analysis time window with stationary plasma conditions is selected. For most discharges, this time window is 1−4 s, as marked by the shaded regions in figure 2. Some discharges are not stationary during this full period, so a more restrictive analysis time window is used. For example, in the reverse field, high density case in figure 2, $v_{C^{2+}}$ takes longer than 1 s to settle down to a stationary value due to $\overline{n}_e$ overshoot, so the time window is 2.5−4 s (marked by the right half of the shaded regions in figure 2). A list of all discharges used in this work is given in the appendix.

The focus of this work is on drift effects in the SOL with attached divertor conditions. The radiated power fraction f_{rad} was typically below 20%, and discharges with $f_{rad} > 40\%$ are not included in the analysis to avoid cases where the plasma begins to detach [23, 24].

Due to ramp-rate limitations of the superconducting coils, as well as programmatic constraints, the forward and reverse field discharges were executed on separate days, about 5 weeks apart. The forward field experiment occurred three weeks after a boronization, while the reverse field experiment occurred immediately after a boronization. The wall conditions were thus cleaner for the reverse field discharges, leading to lower overall impurity concentrations and radiated power, especially in the high density cases [25]. This does not affect the results of this paper but does preclude detailed investigation into how drifts affect the SOL impurity distribution.

2.3. Diagnostics

The primary edge diagnostic used in this work is coherence imaging spectroscopy (CIS), a technique that uses polarization interferometry to provide high-spatial-resolution 2D images of impurity ion flow velocities throughout the SOL [26].

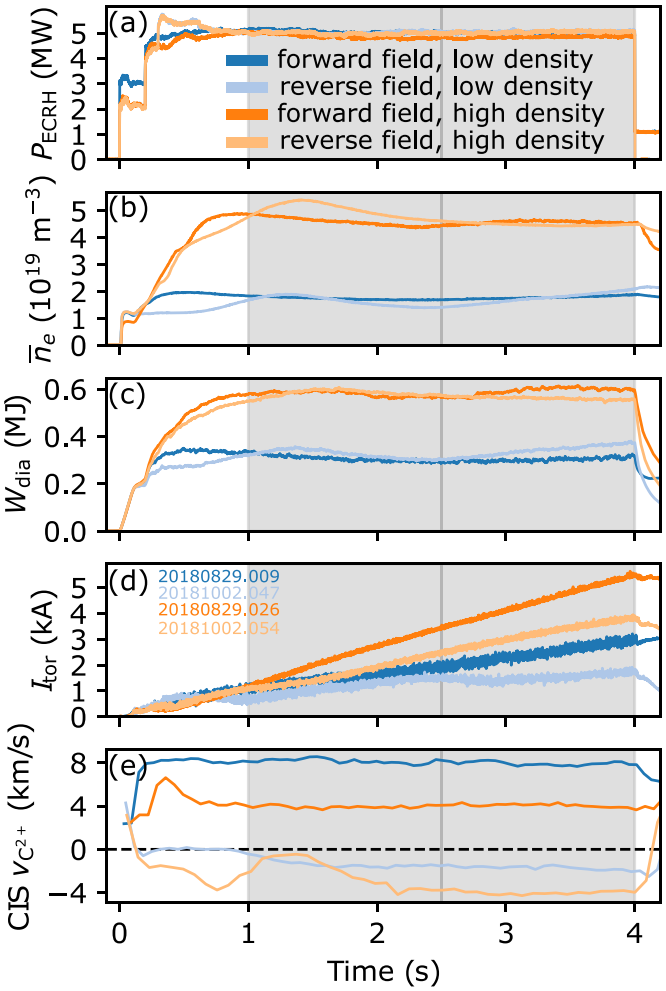

Figure 2. Time evolution of measured parameters for matched forward and reverse field discharges at low and high density: (*a*) electron cyclotron resonance heating power P_{ECRH}, (*b*) line-averaged electron density $\overline{n}_e$, (*c*) diamagnetic stored energy W_{dia}, (*d*) toroidal current I_{tor}, and (*e*) C^{2+} flow velocity $v_{C^{2+}}$ measured by coherence imaging spectroscopy (CIS) near one of the island X-points (see figure 3 for region). The shaded regions denote the stationary period used for diagnostic analysis.

The W7-X CIS system [27] has two views: one looking in the toroidal direction and one viewing vertically through the plasma onto a small portion of a lower divertor target. For this work, only the toroidal viewing system is used since it has a much wider field of view that captures SOL flows throughout multiple islands. Typical exposure times during this experiment were 50−80 ms, providing many tens of images throughout the analysis time window of each discharge. CIS velocity measurements have a systematic uncertainty of ±1−2 km s^{-1} due to the effects of Zeeman splitting and calibration imprecision [27].

During this experiment, CIS was configured to measure emission from the C III line at 465 nm, which is comparatively intense since most of the PFCs are made of graphite. For the SOL parameter range in W7-X, the emission from this line, as calculated via the collisional

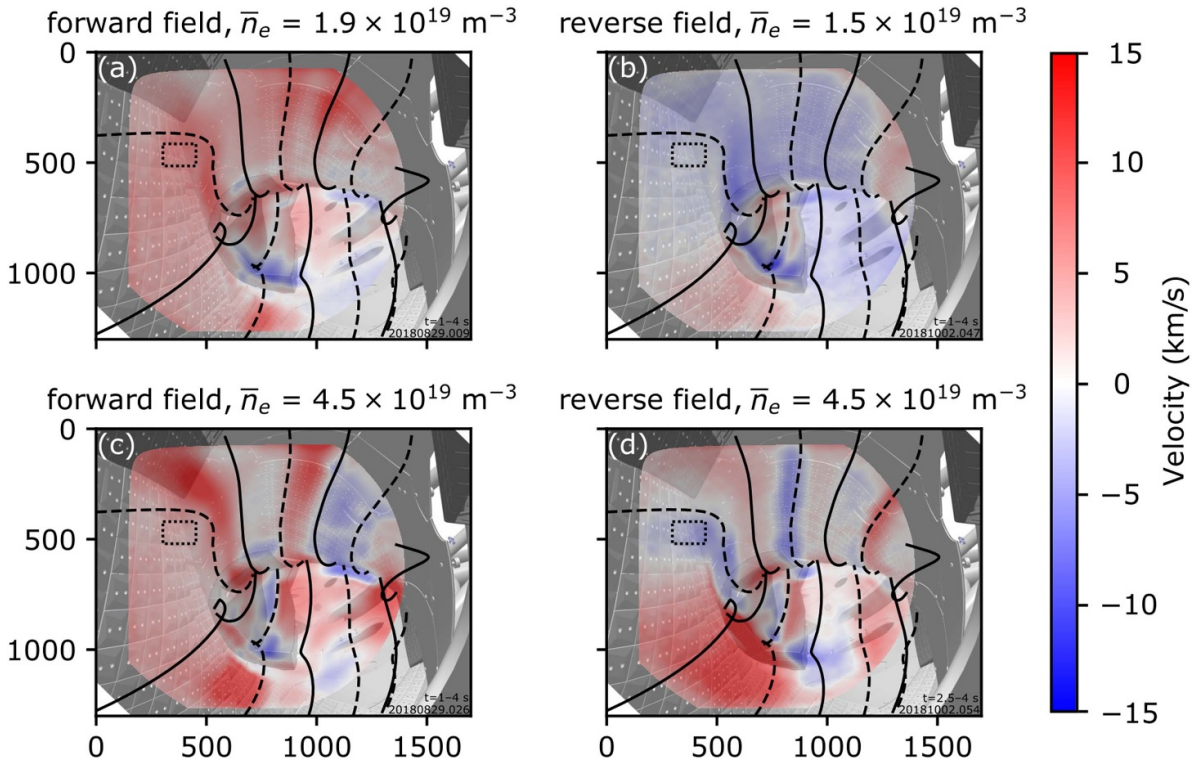

Figure 3. Effect of magnetic field reversal on C^{2+} impurity flow measured by CIS in low-density (*a*), (*b*) and high-density (*c*), (*d*) plasmas. The trajectories of the island O-points (X-points) are overplotted as solid (dashed) black lines, and a CAD view of the in-vessel components is shown in the background. The image axes are labeled by camera pixel number. The black dotted box denotes the region used for the velocity time trace in figure 2(*e*). At low density the flow is largely unidirectional and reverses direction upon field reversal, while at high density counter-streaming flow structures that change upon field reversal are observed.

radiative modeling code ColRadPy [28], is dominated by excitation of C^{2+} (contributions from recombination of C^{3+} and charge-exchange of C^{3+} with hydrogen neutrals are negligible). The measured velocity then corresponds to the velocity of C^{2+} ions. The emission occurs in regions where the electron temperature T_e is in the range of 3−20 eV, with the detailed distribution depending on charge-exchange and transport effects [29]. T_e at the LCFS is always well above this range, so no emission comes from the confined plasma [30]. It has recently been shown that the C^{2+} ion parallel velocity is strongly coupled to the main ion parallel velocity by the friction force throughout most of the SOL parameter range accessible in W7-X [24]. The $\mathbf{E} \times \mathbf{B}$ drift is independent of species charge and mass, so the perpendicular velocity of C^{2+} closely matches the main ion perpendicular velocity. Thus, the CIS-measured velocity is a good proxy for the main ion velocity.

Two arrays of target-embedded Langmuir probes are used to measure n_e and T_e at the divertor targets [31, 32]. One array is on an upper target, and the other is in the stellarator-symmetric position on the lower target in the same module. The probes cover the plasma-target interaction zone in the island SOL, PFR, and target shadowed regions. Thomson scattering is used to measure n_e and T_e just inside the LCFS [33, 34]. The line-averaged density is measured by a dispersion interferometer with 1.33 m path length through the plasma [35]. The diamagnetic energy is measured by diamagnetic loops located at two of the up/down symmetry planes [36]. The radiated power is measured by bolometers [37].

2.4. Basic SOL flow observations

Figure 3 shows CIS-measured SOL flows in forward and reverse field plasmas at low and high density. In each CIS image, the island O-point and X-point trajectories calculated via vacuum field line tracing are displayed as black solid and dashed lines, respectively. The O-point marks the center of the island and the X-point marks the boundary between neighboring passes of the island. Because it is an $m = 6$ island, there are six O-point/X-point trajectories in each image. For convenience we refer to the regions between each pair of X-points as separate islands throughout the rest of this paper, despite the fact that technically they are sections of a single island. Four of the six islands are fully within the field of view. A small portion of one of the remaining islands passes just in front of the plasma facing lens, but contributes negligibly to the velocity. The bottom right island (roughly below pixel row 600 and to the right of pixel column 800) passes in front of steel panels and diagnostic ports, which reflect light that contaminates the flow measurements. The other three islands (on the left side and upper portion of the image) pass in front of the divertors, baffles, or heat shields, which are made of graphite and have

negligible reflectivity. Therefore, throughout this paper only flow measurements from these three islands are used.

As seen in figure 3, reversing the magnetic field for plasmas with similar core parameters substantially affects SOL flows. In the low-density, forward-field case (figure 3(*a*)), the flow is nearly unidirectionally counter-clockwise around the torus when looking from above (positive, red, directed away from the CIS lens) throughout and across multiple islands. The only region where the flow is negative is just above the divertor target and baffle (blue region around pixel row 1000, pixel columns 600−900), where strong flows directed into the target are expected. When the field is reversed (figure 3(*b*)), the flow direction also reverses and is still nearly unidirectional, except above the divertor target and for half of the lower left island. In the high-density cases (figures 3(*c*) and (*d*)) a counter-streaming flow pattern is observed instead of unidirectional flow. This flow pattern changes in a complex way upon field reversal, reversing in some areas while not in others, as first reported in [38]. In all cases, there is little change in the flow pattern just above the divertor target upon field reversal.

The near-unidirectional flow pattern is consistently observed only in the low-iota magnetic configuration at the lowest densities accessible by W7-X. The vast majority of plasmas across different magnetic configurations instead exhibit counter-streaming flows [38], as predicted by edge plasma simulations [3]. The fact that this unidirectional flow pattern largely reverses with field direction implies it is somehow caused by drifts.

3. Forward model for coherence imaging spectroscopy

In this section we investigate the relationship between the 2D flow images obtained by CIS and the complex, 3D flow pattern of particles in the SOL, which includes both parallel and perpendicular components. The main aim is to determine to what extent the flow reversal observation at low density reflects direct measurement of the reversing drift flow vs drifts indirectly modifying the parallel flow.

The principal challenge with interpreting CIS velocity measurements is that they are integrated along sightlines that pass through multiple islands, with a relative orientation to the magnetic field that changes along each sightline's length. Significant effort is required to relate the line-integrated velocities to local flow velocities. For CIS diagnostics on tokamaks, this has been accomplished using tomographic reconstruction of the flow profile, which makes use of the fact that the flow is axisymmetric [39, 40]. However, this approach is not suitable for W7-X owing to the complex 3D geometry of the edge magnetic islands. We thus employ a forward modeling approach by starting with a physically motivated assumed 3D flow profile, generating a synthetic CIS image by integrating the flow profile along the diagnostic sightlines, and then comparing the synthetic data against experimental data.

For each pixel in a CIS image, the measured velocity is approximately given by

$$v_{\mathrm{CIS}} \approx \frac{\int_L \epsilon \mathbf{v}\cdot\hat{\boldsymbol{\ell}}\,\mathrm{d}\ell}{\int_L \epsilon\,\mathrm{d}\ell}, \tag{1}$$

where ϵ is the emission intensity, $\mathbf{v}$ is the velocity of the emitting species, $\hat{\boldsymbol{\ell}}$ is the unit vector directed along the sightline for this pixel, and $\mathrm{d}\ell$ is the differential length along the sightline L. To separate drift flow from the parallel flow, $\mathbf{v}$ is decomposed into components parallel and perpendicular to the magnetic field, so evaluating $\mathbf{v}\cdot\hat{\boldsymbol{\ell}}$ requires information about the local magnetic geometry.

The sightline vector $\hat{\boldsymbol{\ell}}$ for each pixel is determined via geometric camera calibration. The in-vessel components are illuminated, and an image is taken. The 3D machine coordinates of features in this image, e.g. the edge of a divertor target or a diagnostic port, are extracted from a CAD model of W7-X and used to calculate $\hat{\boldsymbol{\ell}}$ for a small number of pixels (typically 20–30) well-distributed across the field of view. Interpolation is then used to calculate $\hat{\boldsymbol{\ell}}$ for the rest of the pixels in the image.

The flow velocity in the island SOL is decomposed as

$$\mathbf{v} = v_{\parallel}\hat{\mathbf{b}} + v_r\hat{\mathbf{r}} + v_n\hat{\mathbf{n}}, \tag{2}$$

where $\hat{\mathbf{b}} = \mathbf{B}/|\mathbf{B}|$, $\hat{\mathbf{r}}$, and $\hat{\mathbf{n}}$ are the unit vectors in the parallel, island radial, and island binormal directions, respectively. The island radial direction is perpendicular to island flux surfaces, pointing away from the island O-point toward the island separatrix. Note that it is not equivalent to the main plasma radial direction, which points away from the magnetic axis. The island binormal direction is perpendicular to both $\hat{\mathbf{b}}$ and $\hat{\mathbf{r}}$. Due to the small field line pitch, it is close, but not equal, to the poloidal direction. The W7-X webservices field line tracer [21] is used to compute $\hat{\mathbf{b}}$ throughout the SOL. Computing $\hat{\mathbf{r}}$ and $\hat{\mathbf{n}}$ is more involved and is accomplished using a recently developed technique based on poloidal sorting of dense Poincaré maps [41].

Using these vectors, the sensitivity of CIS to each flow component is calculated throughout the island SOL. The sensitivities are defined as $S_{\parallel} = \hat{\mathbf{b}}\cdot\hat{\boldsymbol{\ell}}$, $S_r = \hat{\mathbf{r}}\cdot\hat{\boldsymbol{\ell}}$, and $S_n = \hat{\mathbf{n}}\cdot\hat{\boldsymbol{\ell}}$, so that equation (1) can be written as

$$v_{\mathrm{CIS}} \approx \frac{\int_L \epsilon\left(v_{\parallel}S_{\parallel} + v_rS_r + v_nS_n\right)\mathrm{d}\ell}{\int_L \epsilon\,\mathrm{d}\ell}. \tag{3}$$

To determine the region along each sightline that is within the island SOL, a filter based on the connection length is used: points having finite $L_c > 365$ m are in the island SOL, while those with $L_c < 365$ m are in the PFR or target shadowed region. This 365 m cutoff value is determined from the edge connection length map (figure 1(*c*)) by taking the minimum L_c in the island SOL. The SOL-averaged sensitivity for each flow component is shown in figure 4. For most sightlines, the variation of these flow sensitivities throughout the SOL is small, less than 10%, so SOL-averaged values are representative of

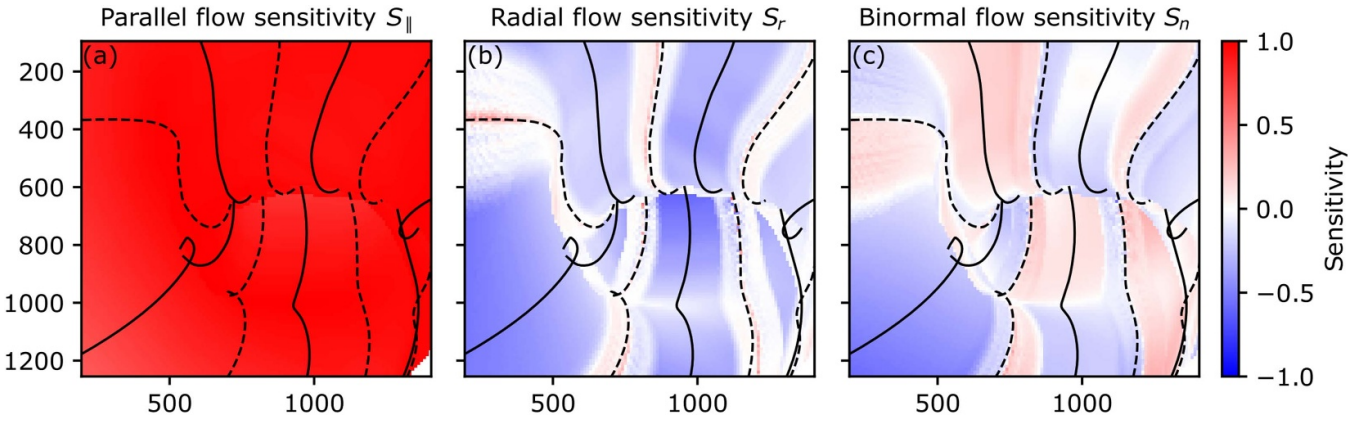

Figure 4. CIS sensitivity to (*a*) parallel, (*b*) island radial, and (*c*) island binormal flows in the island SOL. The trajectories of the island O-points (X-points) are overplotted as solid (dashed) black lines. CIS is most sensitive to parallel flows, and has weaker, non-uniform sensitivity to radial and binormal flows.

the whole SOL. However, near the X-points there is substantial variation, which manifests as the noisier regions in figure 4.

CIS is by far most sensitive to $v_\parallel$, with nearly uniform $S_\parallel > 0.9$ over the entire image (figure 4(*a*)). The positive sign of $S_\parallel$ indicates that a positive parallel flow (counter-clockwise around the torus) will contribute positively to the CIS-measured flow. CIS is much less sensitive to v_r and v_n: the average absolute values of the flow sensitivities are $\overline{|S_r|} \approx 0.2$ and $\overline{|S_n|} \approx 0.15$. The radial flow sensitivity (figure 4(*b*)) is zero near the X-points and negative around the O-points, indicating that a positive radial flow (outward from the island O-points) will contribute negatively to the CIS-measured flow. The binormal flow sensitivity (figure 4(*c*)) flips sign at the X-points and again within each island, but the location where this happens varies from island to island due to variation of the sightline trajectories and path lengths through different islands.

We now turn to the question of whether the unidirectional flow reversal observed at low density (figures 3(*a*) and (*b*)) reflects direct measurement of the reversing perpendicular drift flow or reversal of the parallel flow caused indirectly by drifts. $S_\parallel$ is ∼5 times larger than S_r and S_n, so the drift flow would have to be about 5 times larger in magnitude than the parallel flow to make a similar contribution to CIS measurements. Because S_n flips sign within each island, it is highly unlikely that a binormal drift flow could directly produce a unidirectional flow image. To do so, the drift would have to also reverse within each island in such a way as to cancel the reversal of S_n. As will be discussed in section 4.1, this would require the radial T_e gradient to flip direction within the island, which is physically implausible. In addition, the radial flow sensitivity has the same sign throughout most of the image but shows strong variation near the X-points, which is not reflected in the flow measurements. Thus, it also seems unlikely that radial drift flows could directly produce the observed unidirectional flow pattern. In contrast, $S_\parallel$ is nearly uniform over the entire image, so a uniform $v_\parallel$ could readily produce a unidirectional flow pattern. Taken together, this evidence implies that in the low density cases where flow reversal is observed, CIS primarily measures the parallel flow, not the perpendicular drift flow.

4. Modeling the effects of SOL drifts on parallel flows

The SOL flow measurements at low density imply that drift-induced perpendicular transport alters parallel flows, causing the usual counter-streaming flow pattern to become a near-unidirectional flow pattern. The flow pattern then reverses direction when the field reverses. Motivated by this observation, in this section we develop a simple SOL transport model that includes the effects of drifts in order to understand how they affect parallel flows. This model will be used to help interpret the experimental measurements.

4.1. SOL drifts

The relevant fluid drifts are the $\mathbf{E}\times\mathbf{B}$ drift, $\mathbf{v}_E = \mathbf{E}\times\mathbf{B}/B^2$, and the diamagnetic drift, $\mathbf{v}_{\rm dia} = -\nabla p \times \mathbf{B}/\left(qnB^2\right)$. The $\mathbf{E}\times\mathbf{B}$ drift components in the radial and binormal directions arise for different reasons and have different effects on SOL transport, so they are treated separately. Throughout the rest of this paper we will refer to the binormal component as the 'poloidal $\mathbf{E}\times\mathbf{B}$ drift' to be consistent with existing drift literature [7]. The basic flow patterns of these drifts are depicted in figure 5.

4.1.1. Poloidal $\mathbf{E}\times\mathbf{B}$ drift. The poloidal $\mathbf{E}\times\mathbf{B}$ drift arises from the radial electric field: $v_{E,\theta} = E_r/B$. The direction of E_r is governed by the radial variation of the plasma potential, which largely depends on the T_e distribution since the plasma potential relative to the equipotential divertor surfaces is $V_p \approx 3T_{e,\rm divertor}/e$ [7]. Within the islands, T_e is largest at the island separatrix and decreases moving radially inward, reaching a minimum near the O-point [42]. In the PFR, T_e decays moving radially away from the LCFS [43]. Thus, E_r points toward the O-point within the islands and points away from the LCFS in the PFR.

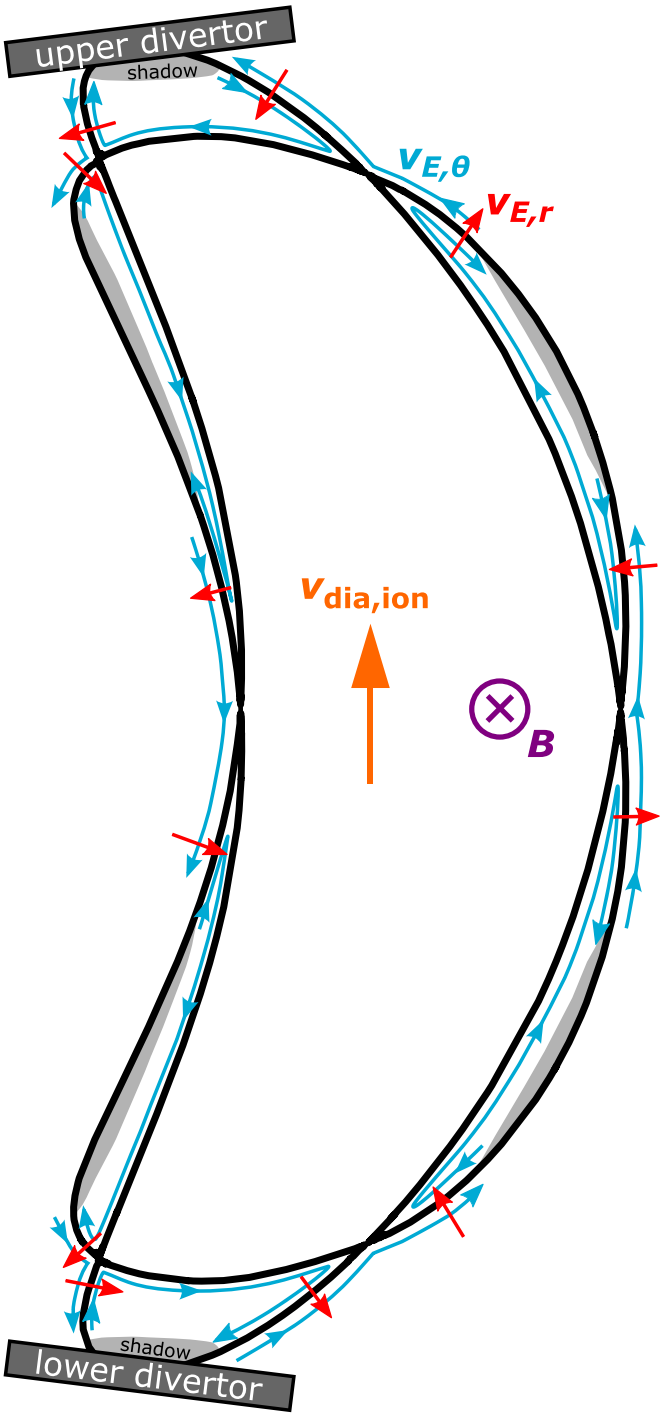

Figure 5. Directions of the poloidal $\mathbf{E}\times\mathbf{B}$ drift $v_{E,\theta}$ (cyan), radial $\mathbf{E}\times\mathbf{B}$ drift $v_{E,r}$ (red), and ion diamagnetic drift $v_{\mathrm{dia,ion}}$ (orange) in the W7-X edge. The magnetic field B points into the page (forward direction); reversing B reverses the direction of all the drifts. The gray region in each island marks the target shadowed region. $v_{E,\theta}$ transports particles poloidally clockwise about the O-point of each island. $v_{E,r}$ transports particles from island to island, effectively forming a counter-clockwise poloidal flow loop passing through the PFR around the main plasma. v_{dia} has a more complex pattern than shown here, but its net effect is largely vertical.

The poloidal $\mathbf{E}\times\mathbf{B}$ drift flow pattern arising from E_r for forward field direction is depicted by the blue arrows in figure 5. In the island SOL, $v_{E,\theta}$ is clockwise about the O-point of each island. The direction of $v_{E,\theta}$ flips across the boundary between the island SOL and PFR. The drift velocity can be estimated as $v_{E,\theta}\approx 3T_{\mathrm{e,divertor}}/(eB\lambda_{T_\mathrm{e}})$, where λ_{T_e} is the radial T_e decay length. At low density the SOL plasma is in the sheath-limited regime and $T_{\mathrm{e,divertor}}\approx T_{\mathrm{e,LCFS}}$, so $v_{E,\theta}$ is large. As density increases and the plasma transitions to the conduction-limited and eventually detached regimes, $T_{\mathrm{e,divertor}}$ decreases substantially, so the poloidal $\mathbf{E}\times\mathbf{B}$ drift becomes weaker.

4.1.2. Radial $\mathbf{E}\times\mathbf{B}$ *drift.* The radial $\mathbf{E}\times\mathbf{B}$ drift arises from a combination of the pre-sheath parallel electric field $E_\parallel$ and toroidicity. Moving along a field line, the parallel potential gradient associated with $E_\parallel$ results in a poloidal potential difference between neighboring passes of the field line. This creates a poloidal electric field $E_\theta=\Theta^{-1}E_\parallel$, where Θ is the internal field line pitch of the island, which represents the distance the field line moves poloidally about the island O-point per unit parallel distance moved along the field line. The resulting drift is then $v_{E,r}=\Theta^{-1}E_\parallel/B$.

From Ohm's law [44],

$$E_\parallel=\frac{j_\parallel}{\sigma_\parallel}-\frac{0.71}{e}\frac{\partial T_\mathrm{e}}{\partial s_\parallel}-\frac{1}{en}\frac{\partial p_\mathrm{e}}{\partial s_\parallel}, \tag{4}$$

where $j_\parallel$ is the parallel current density, $\sigma_\parallel$ is the parallel electrical conductivity, and $s_\parallel$ is parallel distance. Assuming that there are no currents, in the sheath-limited regime $\partial T_\mathrm{e}/\partial s_\parallel=0$, so there is only a weak $E_\parallel$ associated with the $\approx p_\mathrm{e}/2$ pressure drop along the SOL, and $v_{E,r}$ is small. With increasing density, strong parallel T_e gradients develop and $v_{E,r}$ becomes larger. Therefore, one expects the poloidal $\mathbf{E}\times\mathbf{B}$ drift to be dominant at low density and the radial $\mathbf{E}\times\mathbf{B}$ drift to be dominant at high density.

The flow pattern expected from $v_{E,r}$ for forward field direction is shown in figure 5. Generally, $E_\parallel$ points toward the closest target and is largest for the flux tubes near the separatrix in the region between the target and X-point. $v_{E,r}$ then points from the island SOL to the PFR beyond one of the X-points and from the PFR to the island SOL beyond the other X-point. The radial $\mathbf{E}\times\mathbf{B}$ drift can also cause transport within the island either toward or away from the O-point, but this effect is expected to be weaker because $E_\parallel$ decays rapidly moving away from the island separatrix. Interestingly, the net effect of $v_{E,r}$ and $v_{E,\theta}$ is to transport particles and heat from island to island counter-clockwise poloidally around the main plasma.

4.1.3. Diamagnetic drift. The diamagnetic drift flux is composed of the plasma magnetization flux, ∇B drift flux, and curvature drift flux [8]. The magnetization flux is the dominant component but is divergence-free, so it cannot lead to any accumulation or dispersal of particles or energy and therefore has no effect on the SOL plasma distribution [45]. It also has no effect on fluxes to the divertors, as the flux pattern forms a closed loop within the plasma. The ∇B and curvature drift fluxes have non-zero divergence, so they *can* alter the SOL

plasma distribution and divertor fluxes. However, their impact is mitigated because these drifts are largely vertical and are hence averaged out by the helical twist of the island chain [14]. Therefore, the diamagnetic drift is expected to have a weaker direct effect on particle and heat transport than the $\mathbf{E}\times\mathbf{B}$ drift.

An important difference between the diamagnetic and $\mathbf{E}\times\mathbf{B}$ drifts is that the diamagnetic drift has opposite directions for ions and electrons, so it produces a current. For forward field, the non-divergence-free components of the ion diamagnetic drift are vertically upwards (see figure 5), so one would expect a positive current into the upper divertors. As evident from equation (4), this current can alter $E_\parallel$ and thereby modify the radial $\mathbf{E}\times\mathbf{B}$ drift. In this way, the diamagnetic drift can *indirectly* affect particle and heat transport in the SOL.

4.2. Simple SOL model with $\mathbf{E}\times\mathbf{B}$ drifts

The simplest model of the SOL applies to low-density plasmas in the sheath-limited regime, which assumes the plasma is isothermal along each individual flux tube [44]. This corresponds to the regime where CIS observations imply drifts substantially alter parallel flows. To model the effects of drifts on SOL parallel flows, we modify the simple SOL model along similar lines as was done in [7] for tokamaks.

The usual simple SOL model is one-dimensional in the parallel direction. Since drifts by definition have no parallel component, we instead use a 1D model in the island poloidal direction, the geometry of which is shown in figure 6(*a*). The island poloidal coordinate y represents poloidal distance along an island flux surface. It is zero at the position halfway between the upper and lower target shadowed regions, and increases moving toward the upper target shadowed region. The net flow in the island poloidal direction is $v_y = \sin(\theta_\mathrm{p})v_\parallel + \cos(\theta_\mathrm{p})v_{E,\theta}$, where θ_p is the internal field line pitch angle. For the low-iota configuration of W7-X, $\Theta \equiv \sin(\theta_\mathrm{p}) \approx 0.001$, so $v_y \simeq \Theta v_\parallel + v_{E,\theta}$.

The model is symmetric in the helical direction of the islands, i.e. it assumes the divertor targets are helically continuous and does not include the shadowed regions. Effects on the island SOL plasma distribution related to the discontinuous nature of the divertor targets are thus neglected. These effects are expected to be stronger close to the targets and less important in the region between X-points. We assume Θ and $v_{E,\theta}$ do not vary poloidally around each island flux surface. The steady-state 1D island poloidal particle transport equation is then

$$\frac{\mathrm{d}}{\mathrm{d}y}\left[n\left(\Theta v_\parallel + v_{E,\theta}\right)\right] = S_\mathrm{p}, \tag{5}$$

where S_p is the total particle source and $n \equiv n_\mathrm{i} = n_\mathrm{e}$ has been assumed (this is the island divertor analogue to equation (26) in [7]).

In a 1D model, S_p has two components: *true* particle sources/sinks (e.g. ionization and recombination) and *effective* sources/sinks due to cross-field transport. The total particle source is then the sum of the ionization source $S_\mathrm{p,ioniz}$, recombination sink $S_\mathrm{p,recom}$, transport from the main plasma $S_\mathrm{p,main}$, and transport into or out of the SOL by the radial $\mathbf{E}\times\mathbf{B}$ drift $S_{\mathrm{p},v_{E,r}}$. At low density, $S_\mathrm{p,main}$ is important because a substantial number of the recycling neutrals make it to the main plasma before being ionized. For example, for an average SOL density of 1×10^{19} m^{-3}, the neutral penetration length is ≈33 cm [3], which is larger than the ≈10 cm island width. The helical twist of the islands around the main plasma reduces any poloidal or toroidal asymmetries of the particle transport across the LCFS, so we take $S_\mathrm{p,main}$ to be constant between the X-points and zero beyond the X-points, where there is no direct contact with the LCFS. At low density, $S_\mathrm{p,recom}$ is completely negligible, and $S_\mathrm{p,ioniz}$ is weaker than $S_\mathrm{p,main}$, so we neglect its effect on the SOL plasma distribution. In general, $S_{\mathrm{p},v_{E,r}} = -\frac{\mathrm{d}}{\mathrm{d}r}\left[n\Theta^{-1}E_\parallel/B\right]$. At low density, $E_\parallel = -\Theta(\mathrm{d}p/\mathrm{d}y)/(en)$, so

$$S_{\mathrm{p},v_{E,r}} = \frac{\mathrm{d}}{\mathrm{d}r}\left[\frac{1}{eB}\frac{\mathrm{d}p}{\mathrm{d}y}\right] \approx \frac{1}{eBr_\mathrm{i}}\frac{\mathrm{d}p}{\mathrm{d}y}, \tag{6}$$

where $r_\mathrm{i} \approx 10$ cm is the radial island size.

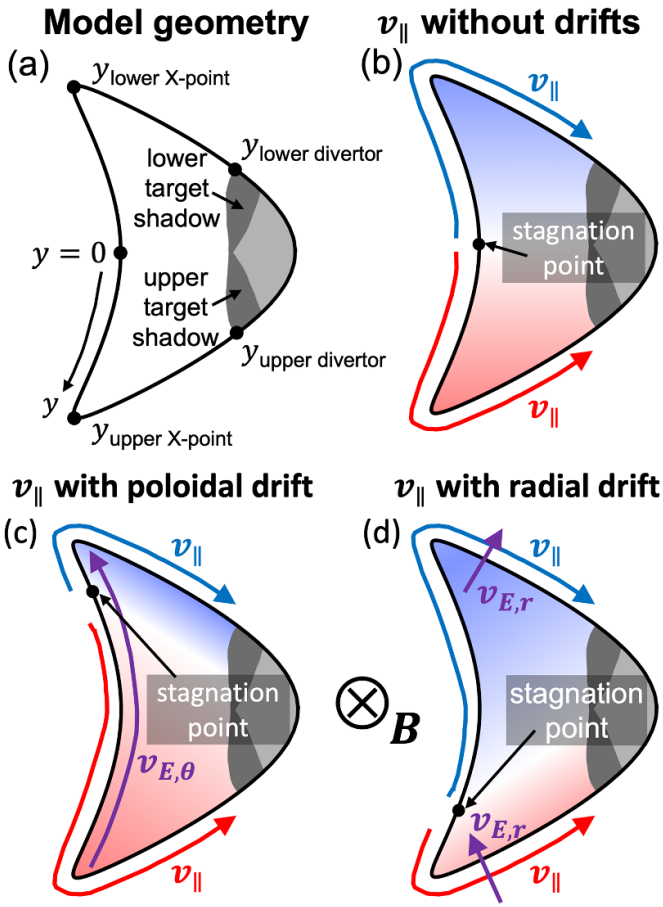

Figure 6. (*a*) Geometry of the simple SOL drift model, which is one-dimensional in the island poloidal direction. (*b*) Distribution of $v_\parallel$ (red: positive flow, counter-clockwise around torus, blue: negative flow, clockwise around torus) throughout the island SOL when no drifts are present. Arrows denote the poloidal component of $v_\parallel$. (*c*) $v_\parallel$ distribution when there exists a poloidal $\mathbf{E}\times\mathbf{B}$ drift clockwise about the O-point (the expected direction for forward field). (*d*) $v_\parallel$ distribution when there exists a radial $\mathbf{E}\times\mathbf{B}$ drift in the expected direction for forward field.

The steady-state 1D island poloidal momentum transport equation is

$$m_{\mathrm{i}}\frac{\mathrm{d}}{\mathrm{d}y}\left[n\left(v_{\parallel}^{2}+\frac{v_{\parallel}v_{E,\theta}}{\Theta}\right)\right]=-\frac{\mathrm{d}p}{\mathrm{d}y}, \tag{7}$$

where m_{i} is the ion mass (this is the island divertor analogue to equation (36) in [7]). The terms on the left-hand side represent the divergence of the island poloidal momentum flux carried by both $v_{\parallel}$ and $v_{E,\theta}$, and the term on the right-hand side represents the pressure gradient force. Equation (7) neglects the effects of currents, viscosity, plasma-neutral friction, and momentum sources/sinks (e.g. charge-exchange reactions). Thus, while the model captures the qualitative effects of drifts on parallel flows, it will generally overestimate the magnitude of $v_{\parallel}$.

With the appropriate boundary conditions, equations (5) and (7) form a coupled set that can be solved numerically for the poloidal n and $v_{\parallel}$ profiles. The boundary condition for $v_{\parallel}$ at the magnetic pre-sheath entrance (MPSE) is $v_{\parallel,\mathrm{MPSE}}=\pm c_{\mathrm{s}}-v_{E,\theta}/\Theta$, where $c_{\mathrm{s}}=\sqrt{T_{\mathrm{i}}+T_{\mathrm{e}}}/m_{\mathrm{i}}$ is the ion sound speed and the $\pm$ denotes sign reversal between the condition at the upper $(+)$ and lower $(-)$ divertors. This is a modified version of the Bohm-Chodura condition that includes an approximate correction for the poloidal $\mathbf{E}\times\mathbf{B}$ drift [46, 47]. Note that at one set of divertors $v_{\parallel}$ and $v_{E,\theta}$ are in the same direction, so $\left|v_{\parallel}\right|<c_{\mathrm{s}}$, while for the opposite set of divertors $v_{\parallel}$ and $v_{E,\theta}$ oppose each other, so $v_{\parallel}$ becomes supersonic before the MPSE.

4.3. Expected drift effects on parallel flow

The simple SOL drift model gives insight into how drifts are expected to affect the density and parallel flow distribution throughout the island SOL. When there are no drifts, the density peaks at the center of the island, halfway between targets. At this point, called the stagnation point, the pressure is maximum, and the pressure gradient force and parallel flow are zero. The pressure decreases moving away from the stagnation point due to the particle sink at the divertor targets. The resulting pressure gradient force then drives a parallel flow toward the closest target. This situation is depicted in figure 6(*b*), where the red/blue color denotes the direction of $v_{\parallel}$. Note that the internal field line pitch has left-handed helicity, so if the poloidal component of $v_{\parallel}$ is clockwise about the O-point, then the toroidal component of $v_{\parallel}$ is clockwise around the torus (blue color). Since the flow direction is governed entirely by the geometry of which target is closest, $v_{\parallel}$ is in one direction over half the island and the opposite direction over the other half.

Figure 6(*c*) shows how this basic picture is modified by the poloidal $\mathbf{E}\times\mathbf{B}$ drift for forward field. The drift transports particles poloidally about the O-point, creating a density asymmetry in the island with higher density in the drift direction. This causes the pressure to peak not at the island center but at a location closer to the X-point in the direction of the drift. The stagnation point then also moves toward the X-point in the direction of the drift. Most of the island is now 'below' the stagnation point, so throughout most of the island $v_{\parallel}$ now points in the counter-clockwise (red) direction. Only in the small portion of the island above the stagnation point does $v_{\parallel}$ still point in the clockwise (blue) direction.

The expected effect of the radial $\mathbf{E}\times\mathbf{B}$ drift on $v_{\parallel}$ for forward field is depicted in figure 6(*d*). Between the lower X-point and lower divertor, $v_{E,r}$ transports particles out of the island SOL and into the PFR (note that the lower X-point/divertor is at the top of the island as depicted in figure 6(*d*)). Between the upper X-point and upper divertor, $v_{E,r}$ instead acts as a particle source into the island SOL. This creates a density asymmetry with higher density near the upper X-point/divertor than the lower X-point/divertor. The stagnation point then shifts toward the upper X-point, so throughout most of the island SOL $v_{\parallel}$ is directed toward the lower divertor, corresponding to clockwise flow around the torus (blue color). The radial $\mathbf{E}\times\mathbf{B}$ drift is thus expected to produce a density asymmetry and stagnation point shift opposite that of the poloidal $\mathbf{E}\times\mathbf{B}$ drift.

As discussed in section 4.1.3, the diamagnetic drift is not expected to directly have a strong effect on the SOL plasma distribution. However, the currents produced by v_{dia} can alter the poloidal electric field, thereby modifying the density asymmetry and stagnation point shift caused by the radial $\mathbf{E}\times\mathbf{B}$ drift. For forward field, v_{dia} is expected to a create a current into the upper divertors and out of the lower divertors. From equation (4), this current enhances $E_{\parallel}$ between the upper X-point and upper divertor but reduces it between the lower X-point and lower divertor. This increases $v_{E,r}$-driven particle transport into the island SOL beyond the upper X-point and reduces the particle transport out of the island SOL beyond the lower X-point. Diamagnetic-drift-driven currents are thus expected to increase the density asymmetry and stagnation point shift caused by the radial $\mathbf{E}\times\mathbf{B}$ drift. Note that when the field direction reverses both the diamagnetic and radial $\mathbf{E}\times\mathbf{B}$ drifts reverse, so the diamagnetic drift still enhances the asymmetries caused by the radial $\mathbf{E}\times\mathbf{B}$ drift (although the asymmetries are in the opposite direction).

4.4. Simple SOL drift model quantitative insights

Figure 7 displays poloidal profiles of n, $v_{\parallel}$, and v_y determined by the simple SOL drift model for a case with forward field ($v_{E,\theta}$ pointing toward the lower X-point as in figure 6(*c*)). The profiles are calculated by numerically solving the particle and momentum transport equations for the simplest case where the radial $\mathbf{E}\times\mathbf{B}$ drift is negligible. In this case there is no radial transport beyond the X-points, so the profiles are flat in these regions. The density profile peaks between the island center and lower X-point, and the density at the lower divertor is larger than at the upper divertor. The stagnation point (where $v_{\parallel}=0$) is near the lower X-point.

The total poloidal velocity v_y is shown scaled by $\Theta^{-1}=1000$ so it can be displayed on the same y-axis scale as $v_{\parallel}$. The location where $v_y=0$ is of interest as it represents the poloidal position in the island where particles have no net movement

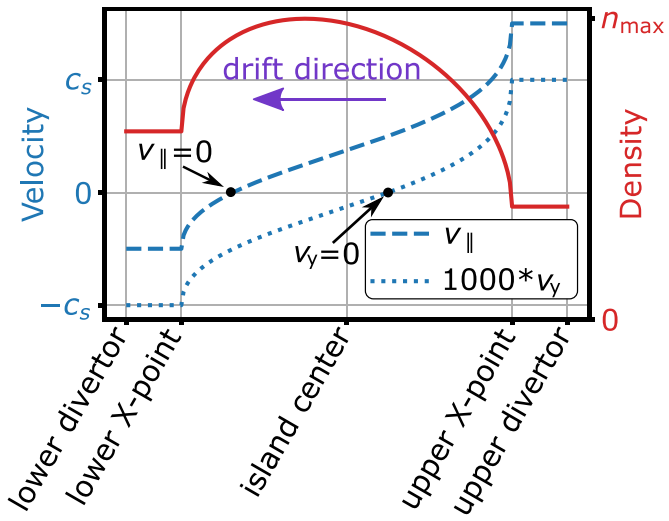

Figure 7. Profiles of n (red solid line), $v_\parallel$ (blue dashed line), and v_y (blue dotted line) predicted by the simple SOL model when there is a poloidal $\mathbf{E}\times\mathbf{B}$ drift with normalized strength $\gamma = 0.25$ pointing towards the lower X-point as in figure 6(*c*) (clockwise about O-point, corresponding to the expected direction for forward field).

toward the targets because the drift motion exactly cancels the parallel motion. This location can be thought of as the 'poloidal flow stagnation point', in an analogous fashion to the usual parallel flow stagnation point. Interestingly, the $v_y = 0$ location is not at the island center, but shifts towards the upper X-point, in the *opposite* direction as the drift. This shift may have implications for impurity transport, as recent modeling work shows that the $v_y = 0$ zone forms a channel for impurities to leak from the divertor region into the main plasma [48].

The density and flow asymmetries in the island can be quantitatively related to the magnitude of the drift velocity $v_{E,\theta}$ by analytically solving equations (5) and (7) (again for the case with the radial $\mathbf{E}\times\mathbf{B}$ drift neglected). Doing so yields the following coupled implicit equations

$$n_*\left(M_\parallel + 2\gamma\right) = \frac{1}{2}\begin{cases}\gamma - 1, & \text{below lower X-point,}\\ \gamma + y_*, & \text{between X-points,}\\ \gamma + 1, & \text{above upper X-point,}\end{cases} \tag{8}$$

$$n_*\left(M_\parallel^2 + 2\gamma M_\parallel + 1\right) = 1 - \gamma^2, \tag{9}$$

where we have introduced the normalized density $n_* \equiv n/n_{\max}$, parallel Mach number $M_\parallel \equiv v_\parallel/c_s$, and normalized poloidal position $y_* \equiv y/y_{\mathrm{x-point}}$. A key parameter in the solution is the normalized drift strength $\gamma \equiv v_{E,\theta}/(2c_s\Theta)$. The drift velocity only enters the solution through γ, and γ captures the fact that drift effects become stronger in configurations with smaller field line pitch. The magnitude of γ is restricted to $|\gamma| \le 0.5$ in this version of the model. At this point, $M_\parallel$ at one of the divertors becomes zero, causing a singularity due to the simplified Bohm-Chodura condition used by the model.

Substituting the Bohm-Chodura condition, $M_{\parallel,\mathrm{upper/lower}} = \pm 1 - 2\gamma$ (+ at the upper divertor, − at the lower divertor), into equation (8) gives an expression for the upper/lower divertor density asymmetry:

$$\frac{n_{\mathrm{upper}}}{n_{\mathrm{lower}}} = \frac{1+\gamma}{1-\gamma}. \tag{10}$$

For reverse field, the drift direction is toward the upper X-point, so $\gamma > 0$ and $n_{\mathrm{upper}} > n_{\mathrm{lower}}$. The inequalities reverse when the field reverses.

Solving for the poloidal position of the stagnation point by substituting $M_\parallel = 0$ into equations (8) and (9) gives

$$y_{\mathrm{stagnation}}/y_{\mathrm{x-point}} = 3\gamma - 4\gamma^3. \tag{11}$$

For small drift strength, the stagnation point shifts in proportion to 3γ, and for strong drifts ($\gamma = 0.5$) it shifts all the way to the X-point. At this point, the drift is so strong that $v_\parallel$ becomes unidirectional throughout the entire island SOL.

Finally, we solve for the poloidal position where the net poloidal motion is zero. Setting $v_y = 0$ gives $M_\parallel = -2\gamma$, and substituting this into equation (8) yields

$$y_{v_y=0}/y_{\mathrm{x-point}} = -\gamma. \tag{12}$$

The $v_y = 0$ position shifts in the opposite direction as the drift with a distance linearly proportional to γ. The weaker scaling of the $v_y = 0$ position shift compared to the stagnation point shift is reflected in figure 7 by the $v_y = 0$ position being closer to the island center. When $\gamma = 0.5$, the $v_y = 0$ position has shifted halfway to the X-point.

These analytic model results strictly apply only to low-density plasmas in the sheath-limited regime. At higher density, the assumption that each flux tube in the SOL is isothermal breaks down, and strong poloidal and parallel temperature gradients develop. To model drift effects in the conduction-limited or detached regimes, energy transport equations must then be included to calculate the poloidal T_i and T_e profiles. These equations are highly nonlinear, which precludes analytic solution and makes numerical solution more challenging. An energy transport equation was included in previous drift modeling of the W7-AS island divertor [14], but that work neglected entirely the parallel flows, which are of central interest for the work here.

Despite the model strictly applying only in the sheath-limited regime, the basic physics mechanism regarding the effect of the poloidal $\mathbf{E}\times\mathbf{B}$ drift on parallel flow should still hold in higher density regimes. Rather than this mechanism breaking down at high density, it just becomes weaker because $v_{E,\theta}$ decreases and effects neglected by the model that counter the $v_{E,\theta}$-induced asymmetry become important. For instance, at high density the poloidal $\mathbf{E}\times\mathbf{B}$ drift is expected to be smaller than the radial $\mathbf{E}\times\mathbf{B}$ and diamagnetic drifts, which induce a density asymmetry and stagnation point shift opposite that of $v_{E,\theta}$.

5. Drift effects on SOL transport

Guided by the predictions of the simple SOL drift model, we now turn to interpreting the experimental data.

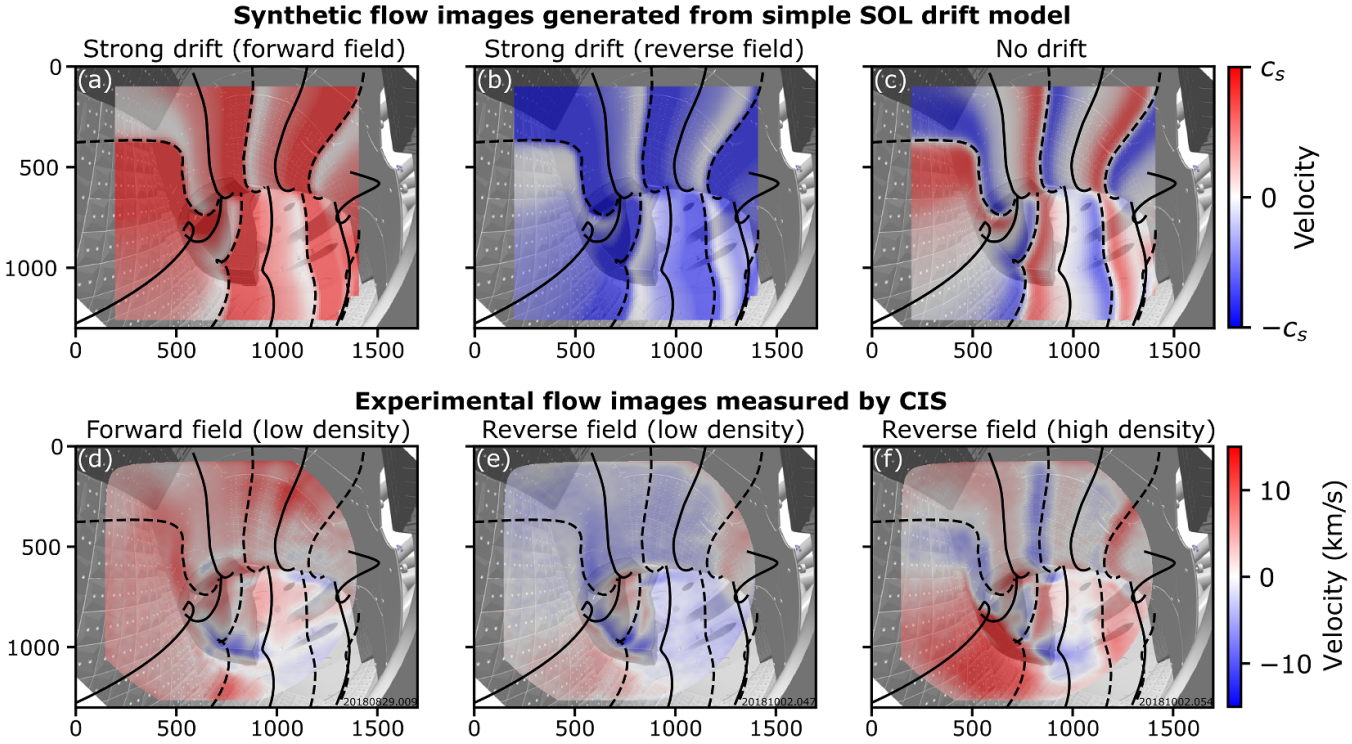

Figure 8. Comparison between synthetic flow images generated by the simple SOL drift model (*a*)–(*c*) and experimental flow images measured by CIS (*d*)–(*f*). The trajectories of the island O-points (X-points) are overplotted as solid (dashed) black lines. At low density both the modeled and measured flow is nearly unidirectional across multiple islands, and the direction of the flow is in agreement for both forward and reverse field. At high density counter-streaming flows are measured, similar to the modeled flow pattern without any drifts.

5.1. Shift of the parallel flow stagnation point

5.1.1. Stagnation point shift to X-points at low density. We start with the CIS observations of unidirectional flow throughout the SOL at low density (figures 3(*a*) and (*b*)). In this density range ($\overline{n}_e < 2\times10^{19}$ m^{-3}), $T_{e,\mathrm{LCFS}} \approx T_{e,\mathrm{divertor}} \approx 90$ eV, so the plasma is in the sheath-limited regime. The predictions of the simple SOL drift model are then expected to apply.

Figure 8 compares experimental CIS measurements against synthetic flow images generated using the simple SOL drift model. Three cases are modeled: one with a strong poloidal $\mathbf{E}\times\mathbf{B}$ drift whose direction matches that expected for forward field (figure 8(*a*)), one with the same drift strength but in the reverse field direction (figure 8(*b*)), and one with zero drift (figure 8(*c*)). The synthetic images are made by first using the simple SOL drift model to calculate the $v_{||}$ profile (as in figure 7). For the no-drift case $\gamma = 0$ is used as an input to the model, and for the drift cases $\gamma = \pm0.5$ is used, which represents the largest possible drift strength in the model and results in the stagnation point shifting all the way to the X-point. The $v_{||}$ profile is then used as an input to the CIS forward model (equation (3) neglecting the radial and binormal components). To do so, the poloidal coordinate y in the simple SOL drift model is mapped to the parallel coordinate z, which represents parallel distance from the center of a field line. The mapping is defined by $z = \Theta^{-1}y$, and a constant $\Theta = 0.001$ throughout the island SOL is used. At each point along the CIS sightlines, z is determined from connection length information using $z = (L_{c,-} - L_{c,+})/2$, where $L_{c,+}$ and $L_{c,-}$ are the parallel distances to the target in the directions counter-clockwise and clockwise around the torus, respectively (note that $L_c = L_{c,+} + L_{c,-}$). The carbon emission intensity is assumed to be uniform throughout the island SOL, but the synthetic flow images are largely insensitive to variation of the emission distribution throughout the SOL.

For forward magnetic field, the synthetic image exhibits near-unidirectional flow in the positive direction (figure 8(*a*)). The stagnation region in each island (white band) is located next to one of the X-points. The structure of the flow in this image is broadly consistent with the experimental forward field CIS flow image (figure 8(*d*)): both exhibit flows that are nearly unidirectional across multiple islands. Moreover, the flow directions in the experimental and synthetic images are consistent in sign. Differences in the detailed structure and magnitude of the modeled and measured flow patterns are unsurprising given the many model simplifications.

When the field reverses, the synthetic image (figure 8(*b*)) has near-unidirectional flow in the negative direction because the stagnation region has shifted to the opposite X-point in each island. The experimental reverse field flow image (figure 8(*e*)) also shows largely unidirectional negative flow, albeit with small regions of positive flow in the lower left and upper right islands. We note that while only two discharges are presented in figures 8(*d*) and (*e*), nearly identical flow patterns are observed by CIS for nine other forward field and six other reverse field low-density discharges.

The average flow velocities are 7 km s^{-1} in forward field and -4 km s^{-1} in reverse field. These values are larger than the $\pm 1-2$ km s^{-1} systematic uncertainty of CIS, so the flow reversal with field direction cannot be attributed to measurement uncertainty. The CIS measurements are thus in agreement with the basic prediction of the simple SOL drift model that the poloidal $\mathbf{E}\times\mathbf{B}$ drift causes the stagnation point to shift poloidally around the island in the drift direction.

The observation of unidirectional flow implies that the stagnation point has shifted substantially toward the divertor, which requires $\gamma = 0.5$ in the simple SOL drift model. γ cannot exceed 0.5 in the model due to the limitations described in section 4.4, so it is possible that $|\gamma| \gtrsim 0.5$ in the experiment. Using $T_{\mathrm{e,divertor}} = 90$ eV and $\Theta = 0.001$ gives $v_{E,\theta} \gtrsim 130$ m s^{-1}, which serves as an estimated lower bound on the drift velocity in these low-density plasmas.

5.1.2. Substantial reduction of stagnation point shift with increasing density. As density increases the measured flow structure transitions from largely unidirectional (figure 8(*e*)) to a counter-streaming pattern (figure 8(*f*)). This transition occurs abruptly at line-averaged densities slightly above 3×10^{19} m^{-3}. The development of a counter-streaming flow pattern implies the drift-induced stagnation point shift has decreased substantially. This is supported by the fact that the modeled flow image for the zero-drift-velocity case (figure 8(*c*)) also exhibits a counter-streaming flow pattern. The effects of poloidal $\mathbf{E}\times\mathbf{B}$ drift transport thus decrease with increasing density, in agreement with expectations.

While the zero-drift modeled flow image (figure 8(*c*)) and high-density measured flow image (figure 8(*f*)) both exhibit a counter-streaming flow pattern, there is a mismatch in the locations and sizes of the flow bundles. This is likely due to a combination of several physics mechanisms lacking from the model, including 1) the development of parallel T_{e} gradients in the conduction-limited regime; 2) flows induced by the remaining radial $\mathbf{E}\times\mathbf{B}$ and diamagnetic drifts; 3) movement of the carbon radiation front, which affects where in the SOL CIS measures $v_{\|}$; 4) flow drive from ionization within the SOL [24]; and 5) possible magnetic topology changes due to β effects.

The transition of the flow structure and accompanying reduction of the poloidal $\mathbf{E}\times\mathbf{B}$ drift appears to be correlated with the transition of the edge plasma from the sheath-limited/low-recycling regime to the conduction-limited/high-recycling regime. Figure 9 shows the dependence of the divertor T_{e} and n_{e} on $\overline{n}_{\mathrm{e}}$ (x-axis) and P_{ECRH} (colorscale) for all discharges from the experiment. Because the density profiles are flat in attached W7-X ECRH discharges [49], $\overline{n}_{\mathrm{e}}$ is essentially a proxy for $n_{\mathrm{e,LCFS}}$. The divertor parameters are taken from the average of the upper and lower Langmuir probes inside the island SOL closest to the strike line (probe 4).

$T_{\mathrm{e,divertor}}$ rapidly drops with increasing density until settling at 20 eV for $\overline{n}_{\mathrm{e}} > 4\times 10^{19}$ m^{-3}. Reliable Thomson scattering measurements of T_{e} near the LCFS were not available for all discharges, but the measurements that were available have $T_{\mathrm{e,LCFS}}$ scattered over 50–120 eV with weak dependence on

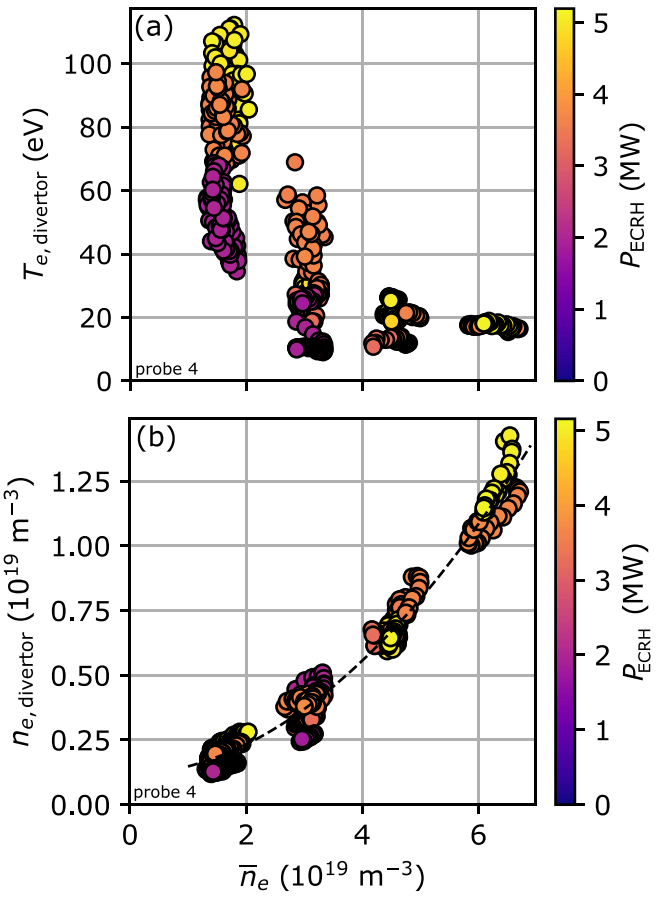

Figure 9. Evolution of the (*a*) divertor electron temperature and (*b*) density with increasing line-averaged density and heating power. The rapid drop of $T_{\mathrm{e,divertor}}$ and superlinear rise of $n_{\mathrm{e,divertor}}$ with increasing $\overline{n}_{\mathrm{e}}$ are signatures of the edge plasma transitioning from the sheath-limited/low-recycling regime to the conduction-limited/high-recycling regime.

density and heating power. The drop of $T_{\mathrm{e,divertor}}$ is thus accompanied by the development of a large parallel T_{e} gradient in the SOL, with $T_{\mathrm{e,LCFS}} - T_{\mathrm{e,divertor}} > 30$ eV for $\overline{n}_{\mathrm{e}} > 4\times 10^{19}$ m^{-3}. This signifies that the edge plasma has transitioned from the sheath-limited regime to conduction-limited regime. $n_{\mathrm{e,divertor}}$ also increases superlinearly with $\overline{n}_{\mathrm{e}}$ in this range, suggesting the plasma is also entering the high-recyling regime [50].

5.1.3. Small stagnation point shift at high density. In high-density plasmas that exhibit a counter-streaming flow pattern, the locations of the flow bundles shift with plasma parameters and field direction. Figure 10 shows that increasing the density in reverse field plasmas causes the flow bundles to rotate counter-clockwise about the image center. In figure 10(*a*), the trajectories of the stagnation points at $\overline{n}_{\mathrm{e}} = 4.5\times 10^{19}$ m^{-3} are marked by dotted lines. In figure 10(*b*), the flow pattern at $\overline{n}_{\mathrm{e}} = 6\times 10^{19}$ m^{-3} is shown with the same lower-density stagnation point trajectories overplotted. This makes it clear that the flow bundles at higher density have rotated slightly counter-clockwise about the image center. For example, the blue flow bundle on the left side of the image has shifted

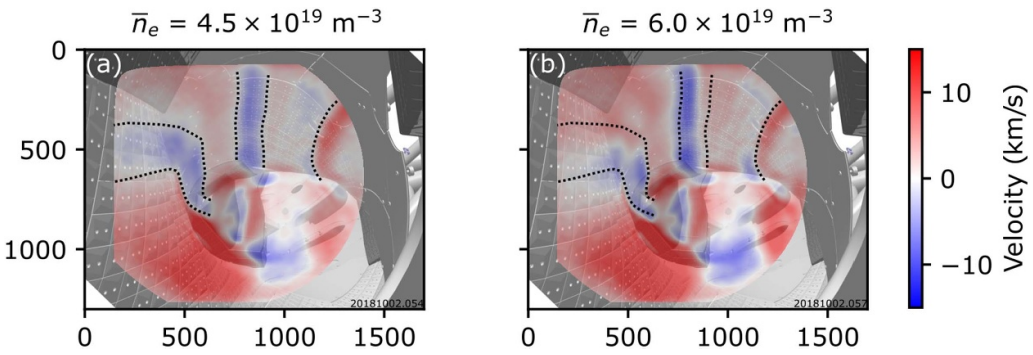

Figure 10. Counter-streaming flow pattern measured by CIS in reverse field plasmas at (*a*) $\overline{n}_e = 4.5 \times 10^{19}$ m^{-3} and (*b*) $\overline{n}_e = 6 \times 10^{19}$ m^{-3}. The trajectories of the stagnation points for the lower density case are traced in black dotted lines on both (*a*) and (*b*), revealing that increasing $\overline{n}_e$ causes the flow bundles to rotate counter-clockwise about the center of the image. A video version of this figure is available that shows rotation of the flow bundles due to changing $\overline{n}_e$ for both forward and reverse field.

downward, while the vertical blue flow bundle near the top of the image has shifted to the left.

Forward field discharges also show rotation of the flow bundles as density varies, but here the rotation direction is opposite: the bundles rotate clockwise about the image center with increasing density (see video version of figure 10). Varying the heating power also causes a similar, but less pronounced, rotation of the flow bundles. The trends are opposite that for density: increasing power causes the bundles to rotate counter-clockwise in forward field and clockwise in reverse field.

The fact that the rotation direction of the flow bundles reverses with field direction implies the rotation is caused by drifts. While the quantitative predictions of the simple SOL drift model do not apply to these high-density plasmas, the basic mechanism that drifts cause the stagnation point to shift poloidally in the island should still hold. For reverse field, the poloidal $\mathbf{E} \times \mathbf{B}$ drift causes the stagnation point to shift counter-clockwise about O-point, which manifests in CIS images as rotation of the stagnation points clockwise about the image center. Recalling that $v_{E,\theta} \propto T_{\mathrm{e,divertor}}$, figure 9 implies that $v_{E,\theta}$ will increase with heating power and decrease with density. So for reverse field, increasing heating power is expected to increase the clockwise rotation of the flow bundles, while increasing density instead causes the flow bundles to rotate counter-clockwise. This is in agreement with the experimental observations. Poloidal $\mathbf{E} \times \mathbf{B}$ drift transport is thus a candidate mechanism for the small stagnation point shift in high-density CIS images. The expected scaling of the radial $\mathbf{E} \times \mathbf{B}$ drift with density and heating power is more difficult to determine, so it remains to be seen whether it could also cause the observed stagnation point shift.

5.2. Upper/lower divertor density asymmetry

We now turn to investigating density asymmetries between the upper and lower targets. The effects of drifts on target heat loads, electron temperature, and ion saturation current, which together are related to density, were previously investigated in [15]. It was found that upper/lower divertor asymmetries in low-density plasmas were qualitatively consistent with the poloidal $\mathbf{E} \times \mathbf{B}$ drift. Here we focus only on the density asymmetry because it can be compared directly against the predictions of the simple SOL drift model.

Figure 11 compares density profiles at the upper and lower targets between forward and reverse field low-density plasmas. The edge magnetic topology based on the vacuum magnetic field is displayed in figure 11(*a*) and indicates for each probe whether it contacts the island SOL, PFR, or target shadowed region. The three probes at largest major radius (probes 1, 2, and 3) contact the PFR. The next outermost two probes (4 and 5) contact the island SOL, with probe 4 right next to the strike line. The group of five probes at smallest major radius (probes 6 through 10) all contact the target shadowed region, but probes 6 and 7 are directly underneath the region of confined field lines around the O-point.

The measured upper/lower density asymmetries are generally consistent with expectations based on the poloidal $\mathbf{E} \times \mathbf{B}$ drift. In the PFR, $v_{E,\theta}$ points away from the lower target probes and toward the upper target probes for forward field and vice-versa for reverse field. One then expects density to be larger at the upper target for forward field and larger at the lower target for reverse field, and this expectation is borne out by the measurements. In the island SOL, the drift is instead expected to cause the lower target density to be higher than the upper target density in forward field and vice-versa in reverse field. The reverse field measurements are consistent with this expectation. For forward field, the density at the strike line (probe 4) shows only a small asymmetry and not in the expected direction, although the asymmetry is small enough to be within the measurement's uncertainty range.

In the target shadowed region the expected drift direction is more uncertain because the T_e distribution is not as well understood. The measurements show an upper/lower divertor density asymmetry that flips around the location of probes 7 and 8. The probes at smaller major radius R measure higher density at the upper target for forward field and higher density at the lower target for reverse field. The probes at larger R, which are close to the O-point, see the opposite. The asymmetry observed by the probes at smaller R is consistent with

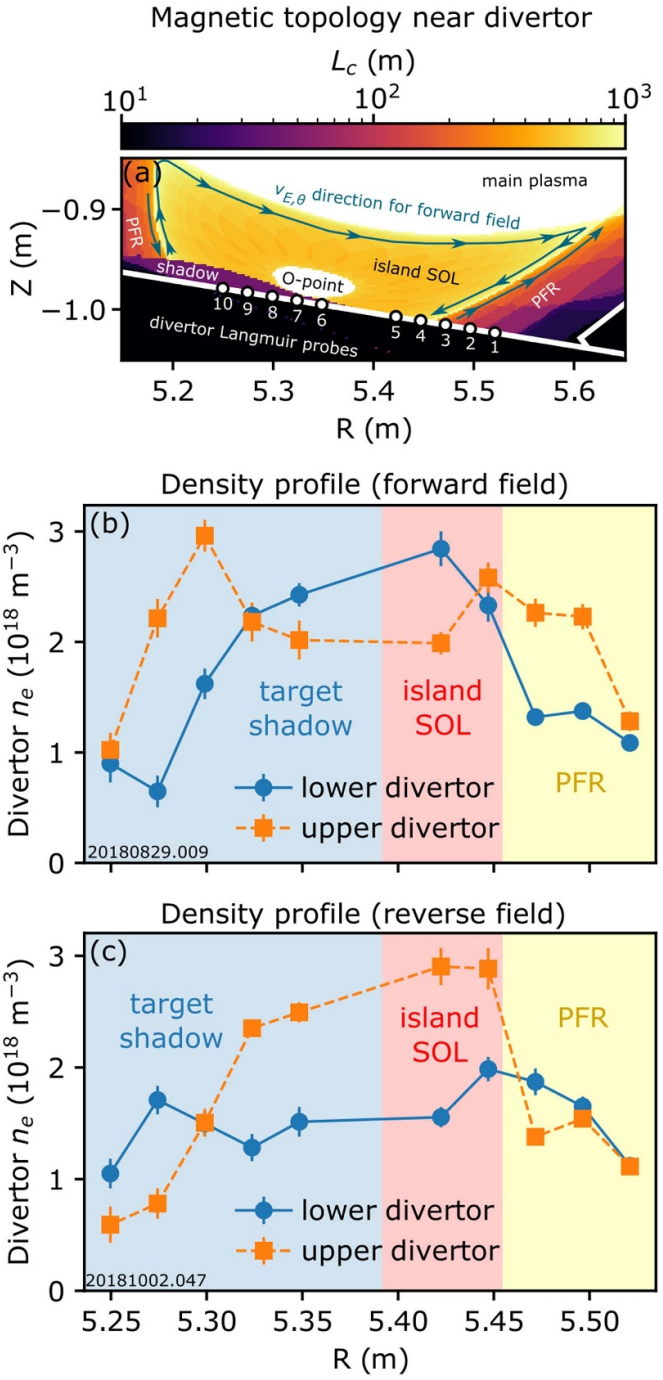

Figure 11. (*a*) Edge magnetic topology near the lower divertor ($\phi = -9°$) based on connection lengths calculated using the vacuum magnetic field. The locations of the Langmuir probes are marked by white circles and the expected poloidal $\mathbf{E} \times \mathbf{B}$ direction in forward field is shown with blue arrows. (*b*), (*c*) Divertor density profiles in low-density plasmas for (*b*) forward field and (*c*) reverse field.

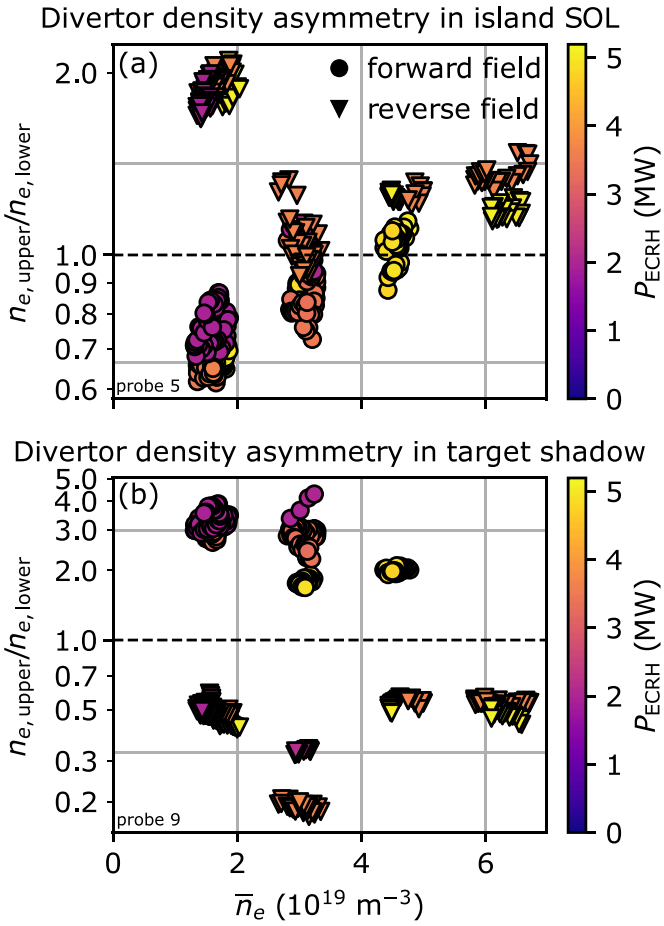

Figure 12. Dependence of the upper/lower divertor density asymmetry on line-averaged density and heating power for locations on the divertor contacting (*a*) the island SOL and (*b*) the target shadowed region. The horizontal dashed black line denotes where $n_{\mathrm{e,upper}} = n_{\mathrm{e,lower}}$, i.e. where there is no asymmetry. Note that the y-axes are logarithmic, so asymmetries with equal magnitude but opposite direction appear the same distance from the dashed black line.

the poloidal $\mathbf{E} \times \mathbf{B}$ drift under the normal assumption that T_e decreases moving away from the island separatrix. The opposite asymmetry observed by the probes near the O-point could be caused by an inversion of the radial electric field, or possibly radial $\mathbf{E} \times \mathbf{B}$ drift transport.

5.2.1. Asymmetry scaling with density. As plasma density increases, the divertor density asymmetry scales differently in different topological regions. Figure 12 shows how the asymmetry, quantified by $n_{\mathrm{e,upper}}/n_{\mathrm{e,lower}}$, varies with line-averaged density and heating power. In the island SOL (figure 12(*a*)) at low density, $n_{\mathrm{e,upper}}$ is twice as large as $n_{\mathrm{e,lower}}$ for reverse field (triangular points) and about two-thirds as large for forward field (circular points). For $\overline{n}_e > 2 \times 10^{19}$ m^{-3} the asymmetry decreases substantially, and there is only a small difference between forward and reverse field discharges. The small remaining asymmetry is still consistent with the poloidal $\mathbf{E} \times \mathbf{B}$ drift, as $n_{\mathrm{e,upper}}/n_{\mathrm{e,lower}}$ tends to be larger in reverse field discharges than in forward field discharges. This reduction of poloidal $\mathbf{E} \times \mathbf{B}$ drift-induced asymmetry with increasing density is consistent with both theoretical expectations and the CIS flow measurements.

In the target shadowed region, the divertor density asymmetry instead persists as line-averaged density increases. As shown by figure 12(*b*), the density asymmetry at probe 9 has little dependence on either line-averaged density or heating power (the reverse field discharge with $\overline{n}_e = 3 \times 10^{19}$ m^{-3} and

$P_{\mathrm{ECRH}} = 3.5$ MW appears to be an outlier). The density asymmetry for other probes in the target shadowed region shows a similar lack of variation with density and heating power. For forward field $n_{\mathrm{e,upper}}/n_{\mathrm{e,lower}} = 2-4$, and for reverse field $n_{\mathrm{e,upper}}/n_{\mathrm{e,lower}} = 0.4-0.6$. The persistence of the divertor density asymmetry even at high $\overline{n}_{\mathrm{e}}$ implies that poloidal $\mathbf{E}\times\mathbf{B}$ drift transport is still important in the target shadowed region, even though it has diminished substantially in the island SOL. However, we note that this conclusion is based on the topological regions determined from the vacuum magnetic field, and the regions may change with increasing density due to β effects.

The simple SOL drift model predicts the density asymmetry to scale with $(1+\gamma)/(1-\gamma)$ (equation (10)). The drift strength in the model is then related to the density asymmetry by

$$\gamma = \frac{n_{\mathrm{upper}}/n_{\mathrm{lower}} - 1}{n_{\mathrm{upper}}/n_{\mathrm{lower}} + 1}. \tag{13}$$

In the island SOL of the low-density high-power discharges, $n_{\mathrm{e,upper}}/n_{\mathrm{e,lower}} \approx 0.7$ for forward field and $\approx$1.9 for reverse field. This corresponds to a drift strength of $\gamma = -0.2$ for forward field and $\gamma = 0.3$ for reverse field. One would expect the drift strengths to have the same magnitude in forward and reverse field discharges with otherwise matched plasma parameters. The reason they differ somewhat might be related to error fields or the lower SOL impurity content in the reverse field discharges due to cleaner wall conditions. Based on these drift strengths, $v_{E,\theta} = 50-80$ m s^{-1} is inferred. This range of values is somewhat lower than the $v_{E,\theta} > 130$ m s^{-1} estimate inferred from the stagnation point shift in CIS images. Several other estimates of $v_{E,\theta}$ are above this range: transport modeling using heat flux width measurements and EMC3-Eirene gives $v_{E,\theta} > 300$ m s^{-1} [51]; measurements of the radial $T_{\mathrm{e,divertor}}$ gradient using Langmuir probes imply $v_{E,\theta}$ is several kilometers per second [15]; and poloidal velocities measured in the PFR using an array of fluctuation probes range from several hundred meters per second up to 1 km s^{-1} [15]. More detailed modeling and measurements will be needed to understand these discrepancies and is left as future work.

6. Summary and conclusions

We investigate the effects of drift-induced perpendicular transport in the island divertor SOL of W7-X. Drift effects are isolated experimentally by comparing measurements of parallel flows throughout the SOL and density at the divertor targets in discharges with opposite field direction but otherwise matched core plasma parameters. The experiment was performed in the low-iota magnetic configuration, which has the longest connection lengths and smallest internal field line pitch of any of the main W7-X configurations, thereby maximizing the impact of drifts on SOL transport. The interpretation of the measurements is aided by comparison to the predictions of a simple SOL drift model.

At low density ($\overline{n}_{\mathrm{e}} < 2\times10^{19}$ m^{-3}), the parallel flow structure measured by CIS in the island SOL is nearly unidirectional and flips direction when the magnetic field is reversed. This observation is found to be explained by poloidal $\mathbf{E}\times\mathbf{B}$ drift transport. The drift induces a poloidal density asymmetry within the islands, with higher density in the drift direction. The resulting change in the pressure distribution alters the parallel flow structure, causing the stagnation point to shift poloidally from the geometric center position of the open magnetic field lines to the X-point in the drift direction. The parallel flow is then unidirectional throughout most of the SOL, explaining the CIS observations.

As density increases, the measured flow structure transitions from nearly unidirectional to a counter-streaming flow pattern. This implies a substantial reduction in the importance of poloidal $\mathbf{E}\times\mathbf{B}$ transport, as the stagnation point shifts back toward the geometric center position between targets. Nevertheless, the drift still has a small effect on the parallel flow at high density, as CIS measures small shifts in the stagnation point that reverse direction upon field reversal and are consistent in direction with poloidal $\mathbf{E}\times\mathbf{B}$ drift transport.

Upper/lower divertor density asymmetries measured by the target Langmuir probes are consistent with poloidal $\mathbf{E}\times\mathbf{B}$ drift transport. In the region of the divertor in contact with the island SOL, the density asymmetry decreases substantially for $\overline{n}_{\mathrm{e}} > 2\times10^{19}$ m^{-3}, implying the poloidal $\mathbf{E}\times\mathbf{B}$ drift weakens. In the region of the divertor that is shadowed by other targets, a strong density asymmetry consistent with poloidal $\mathbf{E}\times\mathbf{B}$ drift transport is observed for all densities probed in this experiment. Thus, while poloidal $\mathbf{E}\times\mathbf{B}$ drift transport is only important in the island SOL at low densities, it is an important transport mechanism in the target shadowed region for a wide range of plasma conditions.

The parallel flow and divertor density asymmetries observed in this work suggest that for all plasma conditions investigated so far, the poloidal $\mathbf{E}\times\mathbf{B}$ drift has a stronger effect on the SOL than the radial $\mathbf{E}\times\mathbf{B}$ and diamagnetic drifts. The latter drifts are expected to induce density asymmetries opposite those of the poloidal drift, but all observed asymmetries are consistent with the poloidal drift. The simple SOL drift model indicates that with increasing density the radial $\mathbf{E}\times\mathbf{B}$ drift becomes stronger, so the observed decrease in poloidal-drift-driven asymmetries with increasing density might be caused in part by the radial drift. However, to stringently test the radial $\mathbf{E}\times\mathbf{B}$ drift picture presented in this work, future experiments that extend to higher density will be required.

This investigation utilizes measurements exclusively from the low-iota configuration. In other W7-X magnetic configurations, such as the standard configuration, drift effects are expected to be weaker because the connection lengths are shorter. Future field reversal experiments will assess the effects of drift transport in different configurations.

Acknowledgments

This work has been supported by US DoE grant DE-SC0014529. This work has been carried out within the framework of the EUROfusion Consortium, funded by the European Union via the Euratom Research and Training

Programme (Grant Agreement No. 101052200 — EUROfusion). Views and opinions expressed are however those of the author(s) only and do not necessarily reflect those of the European Union or the European Commission. Neither the European Union nor the European Commission can be held responsible for them.

Appendix. Drift experiment discharge list

Table A1. Parameters for the discharges used in this work.

Discharge ID	Field direction	$\bar{n}_e$ (10^{19} m^{-3})	P_{ECRH} (MW)	Analysis time window (s)
20180829.005	forward	3.0	5.0	1–4
20180829.006	forward	2.6	5.0	1–4
20180829.007	forward	2.3	5.0	1–4
20180829.008	forward	1.9	5.0	1–4
20180829.009	forward	1.9	5.0	1–4
20180829.010	forward	1.5	3.5	1–4
20180829.011	forward	1.5	3.5	1–4
20180829.012	forward	1.5	3.5	1–4
20180829.013	forward	1.5	2.0	1–4
20180829.014	forward	1.5	2.0	1–4
20180829.015	forward	1.5	2.0	1–4
20180829.016	forward	3.0	5.0	2–4
20180829.017	forward	3.0	5.0	2–4
20180829.018	forward	3.0	3.5	1–4
20180829.019	forward	3.0	3.5	1–4
20180829.020	forward	3.0	2.5	2–4
20180829.021	forward	3.0	3.5	1–4
20180829.022	forward	3.0	2.0	1–3
20180829.023	forward	3.0	2.0	1–2
20180829.024	forward	4.5	5.0	1–4
20180829.025	forward	4.5	5.0	1–4
20180829.026	forward	4.5	5.0	1–4
20180829.027	forward	4.5	3.5	1–3
20180829.028	forward	4.5	3.5	1–4
20180829.029	forward	4.5	2.0	1–4
20180829.030	forward	4.5	2.0	1–4
20181002.038	reverse	1.9	4.0	2–5
20181002.046	reverse	1.5	5.0	1–4
20181002.047	reverse	1.5	5.0	1–4
20181002.048	reverse	1.5	3.5	1–4
20181002.049	reverse	1.5	3.5	1–4
20181002.050	reverse	1.5	1.0	1–4
20181002.051	reverse	1.5	2.0	1–4
20181002.052	reverse	3.0	2.0	3–4
20181002.053	reverse	3.0	3.5	1–4
20181002.054	reverse	4.5	5.0	2.5–4
20181002.055	reverse	4.5	3.5	1.25–2
20181002.056	reverse	6.0	3.5	2–4
20181002.057	reverse	6.0	5.0	2.25–4

ORCID iDs

D.M. Kriete https://orcid.org/0000-0002-3657-2911
V. Perseo https://orcid.org/0000-0001-8473-9002
J.C. Schmitt https://orcid.org/0000-0002-9407-7636
D. Gradic https://orcid.org/0000-0002-6109-9345
K.C. Hammond https://orcid.org/0000-0002-1104-4434
M. Jakubowski https://orcid.org/0000-0002-6557-3497
C. Killer https://orcid.org/0000-0001-7747-3066
R. König https://orcid.org/0000-0002-4772-0051
F. Reimold https://orcid.org/0000-0003-4251-7924
V. Winters https://orcid.org/0000-0001-8108-7774
M.N.A. Beurskens https://orcid.org/0000-0002-3354-0279
S.A. Bozhenkov https://orcid.org/0000-0003-4289-3532
K.J. Brunner https://orcid.org/0000-0002-0974-0457
E.R. Scott https://orcid.org/0000-0002-1389-1151

References

[1] Beidler C. *et al* 1990 Physics and engineering design for Wendelstein VII-X *Fusion Technol.* **17** 148–68
[2] Bosch H.S. *et al* 2013 Technical challenges in the construction of the steady-state stellarator Wendelstein 7-X *Nucl. Fusion* **53** 126001
[3] Feng Y., Sardei F., Grigull P., McCormick K., Kisslinger J. and Reiter D. 2006 Physics of island divertors as highlighted by the example of W7-AS *Nucl. Fusion* **46** 807–19
[4] Renner H., Sharma D., Kißlinger J., Boscary J., Grote H. and Schneider R. 2004 Physical aspects and design of the Wendelstein 7-X Divertor *Fusion Sci. Technol.* **46** 318–26
[5] Feng Y., Kobayashi M., Lunt T. and Reiter D. 2011 Comparison between stellarator and tokamak divertor transport *Plasma Phys. Control. Fusion* **53** 024009
[6] Chankin A.V. *et al* 1994 The effect of B_T reversal on the asymmetries between the strike zones in single null divertor discharges: experiment and theories *Plasma Phys. Control. Fusion* **36** 1853–64
[7] Stangeby P. and Chankin A. 1996 Simple models for the radial and poloidal E × B drifts in the scrape-off layer of a divertor tokamak: effects on in/out asymmetries *Nucl. Fusion* **36** 839–52
[8] Chankin A.V. 1997 Classical drifts in the tokamak SOL and divertor: models and experiment *J. Nucl. Mater.* **241–243** 199–213
[9] Asakura N., Hosogane H., Tsuji-Iio S., Itami K., Shimizu K. and Shimada M. 1996 Field reversal effects on divertor plasmas under radiative and detached conditions in JT-60U *Nucl. Fusion* **36** 795–813
[10] Rozhansky V., Molchanov P., Veselova I., Voskoboynikov S., Kirk A. and Coster D. 2012 Contribution of E × B drifts and parallel currents to divertor asymmetries *Nucl. Fusion* **52** 103017
[11] Jaervinen A. *et al* 2019 Impact of drifts on divertor power exhaust in DIII-D *J. Nucl. Mater.* **19** 230–8
[12] Jaervinen A.E. *et al* 2018 E × B Flux driven detachment bifurcation in the DIII-D tokamak *Phys. Rev. Lett.* **121** 075001
[13] Masuzaki S., Tanaka H., Kobayashi M., Kawamura G. and The LHD Experiment Group 2019 Effects of drifts on divertor plasma transport in LHD *J. Nucl. Mater.* **18** 281–4
[14] Feng Y., Herre G., Grigull P., Sardei F. and W7-AS Team 1998 The effects of field reversal on the W7-AS island divertor at low densities *Plasma Phys. Control. Fusion* **40** 371–80
[15] Hammond K.C. *et al* 2019 Drift effects on W7-X divertor heat and particle fluxes *Plasma Phys. Control. Fusion* **61** 125001
[16] Rognlien T.D., Ryutov D.D., Mattor N. and Porter G.D. 1999 Two-dimensional electric fields and drifts near the magnetic separatrix in divertor tokamaks *Phys. Plasmas* **6** 1851–7
[17] Rozhansky V., Kaveeva E., Molchanov P., Veselova I., Voskoboynikov S., Coster D., Counsell G., Kirk A. and

Lisgo S. (The ASDEX-Upgrade Team and The MAST Team) 2009 New B2SOLPS5.2 transport code for H-mode regimes in tokamaks *Nucl. Fusion* **49** 025007
[18] Coelho A., Loizu J., Ricci P. and Giacomin M. 2022 Global fluid simulation of plasma turbulence in a stellarator with an island divertor *Nucl. Fusion* **62** 074004
[19] Feng Y. *et al* 2014 Recent Improvements in the EMC3-Eirene Code *Contrib. Plasma Phys.* **54** 426–31
[20] Sinha P., Hölbe H., Pedersen T., Bozhenkov S. and (W7-X Team) 2018 Numerical studies of scrape-off layer connection length in Wendelstein7-X *Nucl. Fusion* **58** 016027
[21] Bozhenkov S., Geiger J., Grahl M., Kißlinger J., Werner A. and Wolf R. 2013 Service oriented architecture for scientific analysis at W7-X. An example of a field line tracer *Fusion Eng. Des.* **88** 2997–3006
[22] Neuner U. *et al* 2021 Measurements of the parameter dependencies of the bootstrap current in the W7-X stellarator *Nucl. Fusion* **61** 036024
[23] Feng Y. *et al* 2021 Understanding detachment of the W7-X island divertor *Nucl. Fusion* **61** 086012
[24] Perseo V. *et al* 2021 2D measurements of parallel counter-streaming flows in the W7-X scrape-off layer for attached and detached plasmas *Nucl. Fusion* **61** 116039
[25] Goriaev A. 2022 Study and optimisation of wall conditioning methods on the superconducting stellarator W7-X *PhD Thesis* Ghent University
[26] Howard J. 2010 Coherence imaging spectro-polarimetry for magnetic fusion diagnostics *J. Phys. B: At. Mol. Opt. Phys.* **43** 144010
[27] Perseo V., Gradic D., König R., Ford O.P., Killer C., Grulke O., Ennis D.A. and (W7-X Team) 2020 Coherence imaging spectroscopy at Wendelstein 7-X for impurity flow measurements *Rev. Sci. Instrum.* **91** 013501
[28] Johnson C., Loch S. and Ennis D. 2019 ColRadPy: a python collisional radiative solver *J. Nucl. Mater.* **20** 100579
[29] Samuell C.M. *et al* 2021 Advancements in understanding the 2-D role of impurity radiation for dissipative divertor operation on DIII-D *28th IAEA Fusion Energy Conf.* (*Nice, France, 10–15 May 2021*) (Vienna: IAEA) IAEA–EX–P1/867 (available at: https://conferences.iaea.org/event/214/contributions/17149/)
[30] Krychowiak M. *et al* 2021 Gaussian Process Tomography of carbon radiation in the transition to detached plasmas in the Wendelstein 7-X stellarator *47th EPS Conf. on Plasma Physics Virtual conference* (*21–25 June 2021*) p 1.1026 (available at: http://ocs.ciemat.es/EPS2021PAP/pdf/P1.1026.pdf)
[31] Laube R., Laux M., Ye M.Y., Greuner H. and Lindig S. 2011 Designs of Langmuir probes for W7-X *Fusion Eng. Des.* **86** 1133–6
[32] Rudischhauser L., Endler M., Höfel U., Hammond K.C., Kallmeyer J.P., Blackwell B.D. and (Wendelstein 7-X Team) 2020 The Langmuir probe system in the Wendelstein 7-X test divertor *Rev. Sci. Instrum.* **91** 063505
[33] Pasch E., Beurskens M.N.A., Bozhenkov S.A., Fuchert G., Knauer J., Wolf R.C. and (W7-X Team) 2016 The Thomson scattering system at Wendelstein 7-X *Rev. Sci. Instrum.* **87** 11E729
[34] Bozhenkov S. *et al* 2017 The Thomson scattering diagnostic at Wendelstein 7-X and its performance in the first operation phase *J. Instrum.* **12** 10004–10004
[35] Brunner K.J., Akiyama T., Hirsch M., Knauer J., Kornejew P., Kursinski B., Laqua H., Meineke J., Trimiño Mora H., Wolf R.C. and (The W7-X team) 2018 Real-time dispersion interferometry for density feedback in fusion devices *J. Instrum.* **13** 09002
[36] Rahbarnia K. *et al* 2018 Diamagnetic energy measurement during the first operational phase at the Wendelstein 7-X stellarator *Nucl. Fusion* **58** 096010
[37] Zhang D. *et al* 2010 Design criteria of the bolometer diagnostic for steady-state operation of the W7-X stellarator *Rev. Sci. Instrum.* **81** 10E134
[38] Perseo V., Effenberg F., Gradic D., König R., Ford O., Reimold F., Ennis D., Schmitz O., Sunn P.T. and (The W7-X Team) 2019 Direct measurements of counter-streaming flows in a low-shear stellarator magnetic island topology *Nucl. Fusion* **59** 124003
[39] Silburn S.A. 2014 A doppler coherence imaging diagnostic for the mega-amp spherical Tokamak *PhD Thesis* Durham University
[40] Gradic D., Ford O.P., Burckhart A., Effenberg F., Frerichs H., König R., Lunt T., Perseo V. and Wolf R.C. (ASDEX Upgrade Team, Wendelstein 7-X Team and Eurofusion MST1 team) 2018 Doppler coherence imaging of divertor and SOL flows in ASDEX upgrade and Wendelstein 7-X *Plasma Phys. Control. Fusion* **60** 084007
[41] Schmitt J.C., Kriete D.M., Andreeva T., Geiger J., Grahl M., Schilling J., Thomsen H. and Flom E. 2022 Radial coordinate maps, radial vectors and binormal vectors for 5/6, 5/5 and 5/4 edge island domains in W7-X *Plasma Phys. Control. Fusion* **64** 055022
[42] Barbui T. *et al* 2020 Measurements of plasma parameters in the divertor island of Wendelstein 7-X through line-ratio spectroscopy on helium *Nucl. Fusion* **60** 106014
[43] Killer C., Grulke O., Drews P., Gao Y., Jakubowski M., Knieps A., Nicolai D., Niemann H., Sitjes A.P., Satheeswaran G. and (W7-X Team) 2019 Characterization of the W7-X scrape-off layer using reciprocating probes *Nucl. Fusion* **59** 086013
[44] Stangeby P.C. 2000 *The Plasma Boundary of Magnetic Fusion Devices* (*Plasma Physics Series*) (Bristol: Institute of Physics Publishing)
[45] Chankin A.V. and Stangeby P.C. 1994 The effect of diamagnetic drift on the boundary conditions in tokamak scrape-off layers and the distribution of plasma fluxes near the target *Plasma Phys. Control. Fusion* **36** 1485–99
[46] Stangeby P.C. and Chankin A.V. 1995 The ion velocity (Bohm–Chodura) boundary condition at the entrance to the magnetic presheath in the presence of diamagnetic and $\mathbf{E} \times \mathbf{B}$ drifts in the scrape-off layer *Phys. Plasmas* **2** 707–15
[47] Hutchinson I.H. 1996 The magnetic presheath boundary condition with $\mathbf{E} \times \mathbf{B}$ drifts *Phys. Plasmas* **3** 6–7
[48] Winters V.R. 2022 Impurity leakage mechanisms in the W7-X island divertor under friction-dominated conditions *Nucl. Fusion* submitted
[49] Bozhenkov S. *et al* 2020 High-performance plasmas after pellet injections in Wendelstein 7-X *Nucl. Fusion* **60** 066011
[50] Reimold F. *et al* 2021 Experimental indications of high-recycling and the role of plasma pressure and power dissipation in the detachment evolution at W7-X *28th IAEA Fusion Energy Conf.* (*Nice, France, 10–15 May 2021*) (Vienna: IAEA) IAEA–CN–123/45 (available at: https://conferences.iaea.org/event/214/contributions/17514/)
[51] Bold D., Reimold F., Niemann H., Gao Y., Jakubowski M., Killer C., Winters V.R. and (The W7-X team) 2022 Impact of transport models on local measurements in W7-X using synthetic diagnostics with EMC3-EIRENE and comparison to experimental observations in the W7-X island scrape-off layer (arXiv:2201.06341 [physics])